
Article:
Diaz-delCastillo, M. orcid.org/0000-0001-7719-6839, Palasca, O., Nemler, T.T. et al. (18 more authors) (2023) Metastatic infiltration of nervous tissue and periosteal nerve sprouting in multiple myeloma-induced bone pain in mice and human. The Journal of Neuroscience, 43 (29). pp. 5414-5430. ISSN 0270-6474

https://doi.org/10.1523/jneurosci.0404-23.2023

Metastatic infiltration of nervous tissue and periosteal nerve sprouting in multiple myeloma induced bone pain

Abbreviated title: Myeloma-induced bone pain.

Marta Diaz-delCastillo[1,2,3,4,5], Oana Palasca[6], Tim T. Nemler[1], Didde M Thygesen[1], Norma A Chávez-Saldaña[7], Juan A Vázquez-Mora[7], Lizeth Y Ponce Gomez[7], Lars Juhl Jensen[6], Holly Evans[3,4], Rebecca E. Andrews[3,4,5], Aritri Mandal[3,4,5], David Neves[8], Patrick Mehlen[8,9], James P Caruso[10,11], Patrick M. Dougherty[12], Theodore J Price[10], Andrew Chantry[3,4,5], Michelle A Lawson[3,4], Thomas L. Andersen[2,13,14], Juan M Jimenez-Andrade[7], Anne-Marie Heegaard[1]

[1]Department of Drug Design and Pharmacology, University of Copenhagen, 2100 Copenhagen, Denmark. [2]Department of Forensic Medicine, Aarhus University, 8870 Aarhus, Denmark. [3]Department of Oncology & Metabolism, University of Sheffield, S10 2RX Sheffield, UK. [4]Mellanby Centre for Bone Research, University of Sheffield, S10 2RX Sheffield, UK. [5]Sheffield Teaching Hospitals, S10 2JF Sheffield, UK. [6]Novo Nordisk Foundation Center for Protein Research, University of Copenhagen, 2200 Copenhagen, Denmark. [7]Unidad Académica Multidisciplinaria Reynosa Aztlan, Autonomic University of Tamaulipas, 88740 Reynosa, Mexico [8]NETRIS Pharma, 69008 Lyon, France [9]Apoptosis, Cancer and Development Laboratory- Equipe labellisée 'La Ligue', LabEx DEVweCAN, Centre de Recherche en Cancérologie de Lyon,69008 Lyon, France. [10]University of Texas at Dallas, Department of Neuroscience and Center for Advanced Pain, 75080 Texas, USA. [11]Department of Neurological Surgery, University of Texas Southwestern Medical Center, Dallas, 75390 Texas, USA. [12]Department of Pain Medicine, Division of Anesthesiology; MD Anderson Cancer Center, Houston, 77030 Texas, USA. [13]Department of Clinical Cell Biology, University of Southern Denmark, 5230 Odense, Denmark. [14]Department of Clinical Pathology, Odense University Hospital, 5000 Odense, Denmark.

Corresponding author:

Marta Diaz-delCastillo, PhD, Post-doctoral researcher

E-mail addresses: marta@forens.au.dk. Phone: +45 71832607

Institute for Forensic Medicine, Department of Forensic Medicine

Palle Juul-Jensens Boulevard 99, DK-8200, Aarhus N, Denmark.

Number of pages: 36

Number of figures: 7

Number of tables: 0

Number of words in abstract: 199

Number of words in introduction: 367

Number of words in discussion: 1451

Conflict of interest statement:

The authors declare no competing financial interests.

Acknowledgements

The authors thank Kaja Laursen, Camilla S. Dall and the animal technicians from the Department of Drug Design and Pharmacology at University of Copenhagen. We also thank the patients for providing their time and agreeing to be part of this project. Figures have been made in Biorender.

Abstract:

Multiple myeloma (MM) is a neoplasia of B plasma cells that often induces bone pain. However, the mechanisms underlying myeloma-induced bone pain (MIBP) are mostly unknown. Using a syngeneic MM mouse model, we show that periosteal nerve sprouting of calcitonin-gene related protein ($CGRP^+$) and growth associated protein 43 ($GAP43^+$) fibres occurs concurrent to the onset of nociception and its blockade provides transient pain relief. MM patient samples also showed increased periosteal innervation. Mechanistically, we investigated MM induced gene expression changes in the dorsal root ganglia (DRG) innervating the MM-bearing bone and found alterations in pathways associated with cell cycle, immune response and neuronal signalling. The MM transcriptional signature was consistent with metastatic MM infiltration to the DRG, a never-before described feature of the disease that we further demonstrated histologically. In the DRG, MM cells caused loss of vascularization and neuronal injury, which may contribute to late-stage MIBP. Interestingly, the transcriptional signature of a MM patient was consistent with MM cell infiltration to the DRG. Overall, our results suggest that MM induces a plethora of peripheral nervous system alterations that may contribute to the failure of current analgesics and suggest neuroprotective drugs as appropriate strategies to treat early onset MIBP.

Significance statement:

Multiple myeloma is a painful bone marrow cancer that significantly impairs the quality of life of the patients. Analgesic therapies for myeloma-induced bone pain (MIBP) are limited and often ineffective, and the mechanisms of MIBP remain unknown. In this manuscript, we describe cancer-induced periosteal nerve sprouting in a mouse model of MIBP, where we also encounter metastasis to the dorsal root ganglia (DRG), a never-before described feature of the disease. Concomitant to myeloma infiltration, the lumbar DRGs presented blood vessel damage and transcriptional alterations, which may mediate MIBP. Explorative studies on human tissue support our preclinical findings. Understanding the mechanisms of MIBP is crucial to develop targeted analgesic with better efficacy and fewer side effects for this patient population.

Introduction

Multiple myeloma (MM) is an incurable malignant bone marrow disorder characterized by abnormal immunoglobulemia along with the development of osteolytic bone lesions, hypercalcaemia, renal impairment and anaemia (Kyle and Rajkumar, 2009). Research into the mechanisms of MM has grown exponentially over the last few decades, leading to the introduction of novel therapies such as autologous stem cell transplantation, proteasome inhibitors and immunomodulators as first-line treatment for the disease, which altogether have doubled the median survival time of MM patients (Kumar et al., 2008; Kazandjian and Landgren, 2016). As research attempts to convert MM into a chronic condition, improving the patients´ quality of life becomes crucial. In a 2016 systematic review of symptom prevalence across MM patients, pain and fatigue were listed as the most common complaints with over 70% of patients reporting pain, which was described as severe in over 40% (Ramsenthaler et al., 2016). Moreover, a profound disconnect exists between the patients´ self-reported pain experience and their physicians´ estimation, with recent research suggesting that almost half of attending clinicians underestimate the severity of bone pain in this patient population (Quinn et al., 2022).

Today, pain management in MM patients includes disease-modifying agents targeted to reducing bone disease (i.e. bisphosphonates, denosumab, radiotherapy) and opioids, often in combination with a corticosteroid as adjuvant (Niscola et al., 2010; Coluzzi et al., 2019). On top of well-known side effects of opioids, such as constipation, development of tolerance and risk of addiction, their effect on breakthrough pain, a common occurrence in bone cancer, is limited (Mercadante, 2018). Thus, there is an evident need to unravel the pathogenesis of bone pain in MM, which may lead to mechanism-based strategies to alleviate symptom burden and improve quality of life in a growing patient population.

In a previous study, we established a local, immunocompetent mouse model of myeloma-induced bone pain (MIBP) through intrafemoral transplantation of 5TGM1-GFP cells in C57BL/KaLwRijHsd mice (Diaz-delCastillo et al., 2020b). In this model, we observed the development of pain-like

105 behaviours over time, which were only partially reversed by systemic antiresorptive therapy;
106 moreover, our study showed profound bone marrow denervation at the terminal stages of the model.
107 Here, we elucidate central and peripheral dysregulations driving the onset and maintenance of MIBP.

108 **Materials and methods**

109 *Cell culture*

110 Mouse 5TGM1-GFP cells passaged *in vivo* were grown in suspension in RPMI media containing
111 glutamine and phenol red, 1% penicillin/streptomycin (100U/100µg/ml), 1% sodium pyruvate
112 (1mM), 1% MEM non-essential amino acids and 10% FBS, at 37°C and 5% CO_2. All reagents were
113 purchased from Thermo Fischer Scientific, Denmark.

114 *Animals*

115 Male 5 to 7-weeks-old C57BL/KaLwRijHsd mice from Envigo (Venray, Netherlands) were housed
116 in a temperature-controlled (22 ± 2 °C) room with 50% relative humidity under a 12:12 light:dark
117 cycle (lights on a 07:00 AM). Mice were housed in groups of 4 or 5 in standard individually ventilated
118 $GM500^+$ cages (524 cm^2) in a mouse-dedicated room and allowed to acclimatize >7 days prior to
119 experimental allocation. Cages were enriched with red translucent shelter, an S-brick, paper ropes
120 and corn hidden in the bedding (Tapvei 2HV bedding, Brogaarden, Gentofte, Denmark). Food
121 (Altromin 1314; Brogaarden, Gentofte, Denmark) and water were provided *ad libitum.* Experiments
122 were conducted in accordance with the Danish Act on Animal Experiments (LBK No. 474 of
123 15/05/2014) and approved by the Danish animal Experiments Inspectorate. This manuscript is
124 reported in accordance to the ARRIVE 2.0 guidelines.

125 *Experimental design*

126 In a time-course study, mice were intrafemorally inoculated with 5TGM1-GFP myeloma cells or
127 vehicle, their behaviour analysed over time, and euthanized at two different time-points (i.e. post-
128 surgical day 17 and 24, respectively) by transcardial perfusion before tissue collection. In the
129 transcriptomics experiment, DRGs from 5TGM1-GFP or vehicle-bearing mice were collected and
130 fresh frozen for further RNA extraction and transcriptome sequencing 24 days after surgery. In the

131 NP137 experiment, mice were dosed with NP137 (10 mg/kg, i.p.) or vehicle biweekly, their behaviour
132 analysed over time and euthanized at end-point by transcardial perfusion before tissue collection. All
133 behavioural testing was carried out in a quiet room during the light phase (between 07:00 AM and
134 19:00 PM) by the same researcher, who was blinded to experimental group. Mice were randomized
135 according to baseline burrowing capacity or weight. Good laboratory practices are described in the
136 Supplementary Table S1 (see Supplementary File S1); all materials are available upon request.

137 *Model induction*

138 Mice were anaesthetized with ketamine/xylazine cocktail (85,5 mg/kg Ketaminol vet- MSD Animal
139 Health, The Netherlands- and 12,5 mg/kg Nerfasin vet – Virbac, Kolding, Denmark; i.p.); eye
140 ointment was applied to prevent dryness (Ophta A/S, Actavis Group, Gentofte, Denmark). Upon
141 confirmation of loss of pedal reflex, the mouse was placed on a heating pad, the leg was shaved and
142 disinfected with 70% ethanol, and an incision (<1 cm) was made above the right anterior knee. The
143 retinaculum tendon was slightly displaced, and the patella ligament pushed to the side, exposing the
144 distal femoral epiphysis, where hole was drilled with a 30G needle. Through an insulin needle (0.3
145 mL; BD Rowa Technologies, Lyngby, Denmark), 10-µl of vehicle (Hank Balance Salt Solution,
146 Gibco, Denmark) or cell suspension ($5x10^4$ 5TGM1-GFP cells) were inoculated into the
147 intramedullary femoral cavity. The hole was closed with bone wax (Mediq Danmark A/S, Brøndy,
148 Denmark), the patella pushed back into place, and the incision closed with surgical clips (Agnthos,
149 Lidingö, Sweden). Mice received 0.5 mL saline (s.c.) and two bolus injections of carprofen (5mg/kg,
150 s.c.; Pfizer, Ballerup, Denmark), one before surgery and another 24 h after.

151 *Limb use*

152 The limb use of freely walking animals was scored as: 4= normal gait; 3= insignificant limping; 2=
153 significant limping and shift in bodyweight distribution towards the healthy limb; 1= significant
154 limping and motor impairment; 0= paraplegia, as previously described (Diaz-delCastillo et al.,
155 2020b). Briefly, mice were acclimatized with their cagemates to a standard transparent cage of 125 x

266 x 185 mm for ≥10 min. Then, mice were individually transferred to a similar cage where their gate was observed for 3 min.

Burrowing

Burrowing capacity was assessed as amount of sand (0-3 mm diameter, ScanSand, Herlev, Denmark) displaced from a burrowing apparatus during a 2-hour burrowing session (Sliepen et al., 2019). The burrowing apparatus consisted of a grey opaque plastic tube (200 mm x 72 mm diameter; frontal end raised 30 mm from the ground) filled with 500 g of sand and placed in a transparent plastic cage (125 x 266 x 185 mm) without bedding, closed with a grid lid. Prior to baseline measurements, mice were placed in pairs in the cage containing an empty burrowing apparatus for 2 h. On the second and third day, this procedure was repeated but the burrowing tube was filled with 500 g of sand. Throughout the experiment, burrowing was conducted at the same time and in the same room in absence of the researcher.

Tissue extraction and analyses

Mice were deeply anaesthetized with a ketamine/xylazine cocktail, as described. Upon loss of pedal reflex, mice were pinned down on their dorsal side and their abdomen and thoracic cage were opened, exposing the beating heart. Transcardial blood was collected with a 27G needle, before transcardially perfusing with 21-28 ml of ice-cold PBS and 4%PFA-0,12% picric acid (Merck, Søborg, Denmark). Spleens were excised and weighed. Ipsilateral femurs were collected, post-fixated 24 h in 4% PFA and stored in 70% ethanol until µCT analyses were performed, and in 0.1M PBS afterwards. Spinal cords and lumbar DRGs were post-fixated 24 h in 4%PFA-0,12% picric acid, dehydrated in 30% sucrose and embedded in OCT (Sakura, Japan). In the transcriptomics experiment, mice were perfused with 10-ml of ice-cold PBS and their lumbar DRGs quickly extracted and fresh-frozen in RNAse-free Eppendorf tubes in a 3-Methylbutanol freezing bath.

Serum IgG_{2b} analyses

180 Blood was left undisturbed at RT for 30-90 min and thereafter centrifuged 10 min at 4 °C and 6000
181 RPM. Serum was stored at -80°C and IgG_{2b} was measured with a sandwich ELISA kit (Bethyl
182 Laboratories, #E99-109; AB_2892024) following manufacturer´s recommendations.

183 *µCT analyses*

184 Ipsilateral femurs were analysed in a SkyScan 1272 ex vivo scanner at 50 kilovots (kV) and 200 mA,
185 as previously described (Lawson et al., 2015). A 0,5 mm aluminium filter and a pixel size of 4,3 mm^2
186 were used. Following standard guidelines (Bouxsein et al., 2010), the following morphometric
187 parameters were assessed: bone volume per total volume (BV/TV), bone surface per bone volume
188 (BS/BV), bone surface per total volume (BS/TV), trabecular thickness (Tb.Th), trabecular spacing
189 (Tb.Sp), trabecular number (Tb.N) and lesion area. Representative 3D models were recreated with
190 ParaViewSoftware (Clifton Park, NY, USA). For the anti-netrin experiments, scans were
191 reconstructed using NRecon software (version 1.6.1.1; SkyScan) within a dynamic range of 0 to 0.15
192 and a ring artifact reduction factor of 5%. Reconstructed images were analyzed using CTAn (version
193 1.9.1.1 Bruker, Belgium). Analysis was done on the cross-sectional images of the tibias or femurs at
194 1.2 mm (offset) from the distal break in the growth plate (reference point), on a fixed 1-mm region.
195 The trabecular bone was carefully traced on all cross-sectional images of the distal femur and BV/TV
196 was calculated.

197 *Immunohistochemistry in lumbar DRGs*

198 Lumbar DRGs were serially sectioned at 16-µm thickness. Slides were washed thrice, permeabilized
199 in 0.1% Triton X-100/T-PBS and blocked with 1% BSA or 3% NDS before antibody labelling against
200 activating transcription factor 3 (ATF3; either 1:200 polyclonal, rabbit anti-mouse, Novusbio,
201 Abingdon, United Kingdom; #NBP1-85816, AB_11014863, or 1:400 polyclonal, rabbit anti-mouse,
202 Santa Cruz, Dallas, Texas; #SC-188, AB_2258513), tyrosine hydroxylase (TH), a marker for post-
203 ganglionic sympathetic neurons (TH polyclonal rabbit anti-mouse; 1:1000, Millipore; #AB152,
204 AB_390204), CD31, a marker of blood vessel endothelial cells (CD31 monoclonal rat anti-mouse,
205 1:500, BD Pharmingen , San Diego, CA; #557355, AB_396660), or GFP (GFP polyclonal chicken

206 anti-mouse; 1:2000, Invitrogen; #A10262, AB_2534023). After, slides were washed and incubated 3
207 h with secondary antibodies: Alexa Fluor 488 (Anti-rabbit, 1:1000, Invitrogen, Themo Fisher
208 Scientific, Slangerup Denmark, #A11008, AB_143165), Cy3 (monoclonal donkey anti-rabbit 1:600;
209 Jackson ImmunoResearch; #711-165-152, AB_2307443), Cy2 (polyclonal donkey anti-chicken,
210 1:400; #703-225-155, AB_2340370). Sections were counterstained with DAPI (1:10,000, Sigma
211 Aldrich; #D21490) for 5 min, dehydrated in an alcohol gradient and rinsed in xylene. Slides were
212 mounted DPX or fluorescent mounting medium containing DAPI (DAKO Agilent, Glostrup,
213 Denmark).

214 *DRG neuronal profile quantifications*

215 Serial DRG sections were separated by >120 µm to prevent duplicate counting of neuronal cell
216 bodies. At least a confocal image from three different sections under a 20X objective per animal was
217 taken on a Zeiss LSM 800 confocal microscope (Jena, Germany). The number of $ATF3^+$ or TH^+
218 immunoreactive neuronal profiles in sensory ganglia were determined in Image J (NIH), as previously
219 reported (Peters et al., 2005), by quantifying both labelled and non-labelled neuronal profiles.

220 *DRG blood vessel quantifications*

221 Quantification was performed by counting the number of $CD31^+$ blood vessels per unit volume (area
222 x thickness) (Ireland et al., 1981; Glaser et al., 2004; Jimenez-Andrade et al., 2008), where blood
223 vessels were identified as $CD31^+$ and 2–10 µm in diameter; $CD31^+$ branched blood vessels were
224 counted as one single vessel (Weidner et al., 1991).. DRG sections were initially scanned at low
225 magnification (10×) to identify the areas with the highest density of $CD31^+$ blood vessels and then a
226 confocal image was obtained at 40× magnification. At least three pictures per animal were taken. An
227 extended depth of focus processing was performed on all Z-stack files for each image and total number
228 and length of $CD31^+$ blood vessels within cell body-rich areas (Hirakawa et al., 2004) were
229 determined using Image J (NIH). Then this area was multiplied by the thickness of the section (16
230 µm).

231 *Immunohistochemistry in femurs*

232 Following µCT, femurs were decalcified in 10% EDTA for two weeks at 4°C prior to cryoprotection
233 in 30% sucrose and 4°C storage; decalcification was monitored using a portable x-ray equipment
234 (Fona X70, Fona, Assago, Italy). Femurs were longitudinally cut in a frontal plane (25-µm thickness)
235 with a cryostat (Leica 1900, Leica Biosystems, Il, USA), mounted on slides (Superfrostplus, Thermo
236 Scientific; #J1800AMNZ) and allowed to dry (30 min, RT). Subsequently, slides were placed in
237 vertical chambers (Shandon, Sequenza Immunostaining, Fisher Scientific; #73-310-017), washed,
238 blocked (3% normal donkey serum, 0.3% triton X-100 in PBS) for 2 h RT and incubated o/n with a
239 primary antibody cocktail containing anti-GFP antibody (polyclonal chicken anti-GFP, 1:2000;
240 #A10262, AB_2534023; Thermo Fisher Scientific, Rockford, IL, USA) , anti-TH antibody (TH
241 polyclonal rabbit anti-mouse; 1:1000, Millipore; #AB152, AB_390204), and an antibody against
242 calcitonin gene-related peptide (CGRP; polyclonal rabbit anti-rat, 1:5000; #C8198, AB_259091;
243 Sigma-Aldrich, St. Louis, MO, USA) or growth associated protein-43 (GAP43; rabbit anti-GAP43;
244 1:1000; #AB5220, AB_2107282; Millipore, Billerica, MA, USA). Subsequently, sections were
245 washed and then incubated 3 h with a secondary antibodies cocktail of Cy3 donkey anti-rabbit (1:600;
246 Jackson ImmunoResearch; #711-165-152, AB_2307443) and Cy2 donkey anti-chicken (1:400;
247 Jackson ImmunoResearch; #703-225-155, AB_2340370). Slides were counterstained with DAPI for
248 5 min (1:20,000, Sigma Aldrich; #D21490), washed, dehydrated through an alcohol gradient and
249 xylene, and sealed with DPX mounting medium (Slide mounting medium; Sigma-Aldrich; #06522).
250 *Quantification of the density of nerve fibers on femoral periosteum and neuroma identification*
251 For quantifications of $CGRP^+$ and $GAP43^+$ nerve fibers density, at least three sections of each mouse
252 femur were analyzed by the same researcher, blinded to model allocation and treatment group. The
253 areas with the highest density of nerve fibers at the metaphyseal periosteum were identified using a
254 10x objective. In all cases, these areas were located within 0.5 mm-1 mm distance from the distal
255 femoral growth plate. Subsequently, a confocal image was obtained using the Z-stack function from
256 a Carl Zeiss confocal microscope (model LSM 800, Jena, Germany). At least three images were
257 obtained for each marker (20× magnification). The Z-stacked images were analyzed with ImageJ and

258 nerve fibers were manually traced to determine their total length using the freehand line tool. Area of
259 evaluation was manually determined tracing the area of the periosteum. This area was multiplied by
260 the thickness of the section (25 um). Results were reported as the density of nerve fibers (total length)
261 per volume of periosteum (mm^3) (Mantyh et al., 2010).
262 For the identification of neuroma-like structures, the following three criteria was followed 1)
263 disordered mass of blind-ending axons ($CGRP^+$) that had an interlacing and/or whirling morphology,
264 2) structure with a size of more than 10 individual axons that is at least 20 µm thick and 70 µm long,
265 and finally 3) a structure that is never observed in the periosteum of normal bone (Devor and Wall,
266 1976; Sung and Mastri, 1983).
267 *Evaluation of human bone*
268 Trephine iliac crest bone biopsies from newly diagnosed MM patients were collected at Sheffield
269 Teaching Hospital upon informed consent and under approval from the East Midlands-Derby
270 Research Ethics Committee, UK (REC19/YH/0319). Needle (3 mm) biopsies were collected under
271 local lidocaine anaesthesia by a qualified medical practitioner as routine standard of care. Biopsies
272 were formalin-fixed o/n, decalcified in formic acid, and paraffin embedded before sectioning at 3,5-
273 µm thickness onto DAKO IHC Flex tissue slides (DAKO Aps, Glostrup, Denmark). Sections were
274 deparaffinized in a xylene and alcohol gradient and subjected to antigen retrieval in Tris-EDTA buffer
275 (pH 9.0) o/n. Slides were washed, blocked for endogenous peroxidases and blocked for unspecific
276 staining 20 min in 5% casein/TBS. Sections were labelled with a rabbit anti-PGP9.5 antibody (Sigma
277 Aldrich, Søborg, Denmark; #SAB4503057, AB_10761291), detected with polymeric alkaline
278 phosphatase conjugated anti-rabbit IgG (BrightVision DPVR-AP, Immunologic) and visualized with
279 stay red (DAKO, Glostrup, Denmark). Next, sections were labelled with a mouse mAb against CD34
280 (Abcam, Cambridge, UK; #ab78165, AB_1566006), detected by polymeric horse radish peroxidase
281 conjugated anti-mouse IgG (BrightVision DPVR-HRP, Immunologic) and visualized with deep space
282 black (DSB, CCC). Sectioned were then blocked with mouse serum and labelled with a mouse mAb
283 against CD138 (BD Pharmnigen, Allschwil, Switzerland; #552723, AB_394443), which was detected

284 with horse radish peroxidase conjugated anti-fluorescein Fab fragments (Merck, Darmstadt,
285 Germany) and visualized with diaminobenzidine (DAB^+; DAKO, Glostrup, Denmark). Finally,
286 sections were counterstained with Mayer´s haematoxylin and mounted in Aquatex (Merck,
287 Darmstadt, Germany). Slides were brightfield scanned with a 20x objective in an automated VS200
288 Slidescanner (Olympus Microscopy, Japan) and analysed in VS200 Desktop, (Olympus) by an
289 experimenter blinded to the slide origin.

290 *Mouse transcriptomics sequencing and analyses*

291 In the transcriptomics experiment, 20 male C57BL/KaLwRijHsd mice underwent inoculation of
292 5TGM1-GFP cells or vehicle as described. Pain-like behaviours were assessed over time and mice
293 were euthanized 24 days after surgery by transcardial perfusion with 10 ml of ice-cold PBS. Serum
294 samples were collected and processed for IgG_{2b} assessment as described. Ipsilateral whole DRG
295 lumbar L2-L4 were snap frozen in RNAse free Eppendorf tubes in a 3-Methylbutanol freezing bath.
296 Tissue was homogenized in a bead miller and total RNA was extracted with a Qiagen RNAse microkit
297 (Qiagen, Copenhagen, Denmark). RNA quality was assessed with an Agilent Bioanalyzer and
298 samples with a RIN <8.0 were excluded (n=2).

299 Remaining samples underwent DNBSEQ transcriptome sequencing by BGI Denmark (BGI,
300 Copenhagen, Denmark). Fastq files with reads with adaptors removed were further used in the
301 bioinformatics analysis upon filtering out low quality ends. We used Salmon (version 1.5.2) (Patro et
302 al., 2017) to quantify transcript expression, using as reference the mouse cDNA set (coding and non-
303 coding transcripts) corresponding to GRCm39. The salmon index was built using the corresponding
304 GRCm39 genome as decoy sequence. Both the cDNA set and genome were obtained from Ensembl,
305 release 104 (Howe et al., 2020; Cunningham et al., 2021). Gene-level expression estimates were
306 further obtained using the tximport R package (Soneson et al., 2015). Genes with non-zero counts in
307 at least 3 samples and with at least 10 estimated mapped reads in at least one of the samples were
308 retained for further analysis. Differential expression analysis between the MM and sham was
309 performed using the Wald test from DESeq2 R package (Love et al., 2014).

310 Metastatic infiltration of MM cells within the DRG was assessed from the sequencing reads by
311 counting the reads mapping to the eGFP, an artificial transfect to the 5TGM1 cell line. Bbduk (bbmap
312 suite, v. 38.90 (Bushnell) with a kmer size of 31 was used to find the proportion of eGFP matching
313 reads in each sample; eGFP sequences retrieved from (SnapGene).
314 GSEA (gene set enrichment analysis) for GO biological processes terms and reactome pathways was
315 performed using the R packages clusterProfiler (Sacks et al., 2018) and ReactomePA (Yu and He,
316 2016). Genes were ranked using the Wald test statistic (stat value) provided by DESeq2. We used the
317 pairwise_termsim() function from enrichplot (Yu, 2019) to obtain the jaccard similarity coefficient
318 (JC) in terms of overlapping gene sets between each two terms. Whenever JC was >0.7, we selected
319 only the term with lowest adjusted p-value value in our enrichment results. Visualizations of the
320 enrichment results were produced using the R packages DOSE (Yu et al., 2015) and enrichplot (Yu,
321 2019) and data is accessible in GEO under accession code GSE216802.
322 We compared our MM mouse data with DRG expression data from 6 other mouse models of painful
323 conditions, as described in Bangash et al (Bangash et al., 2018). The transcriptomes of DRGs from
324 the test mice and their corresponding sham had been profiled using the Affymetrix GeneChip Mouse
325 Transcriptome Array 1.0 and obtained from Additional file 3 (Bangash et al., 2018). We compared
326 our model with the 6 models in terms of overlap and direction of differentially expressed genes, as
327 well as in terms of GSEA results. For our MM model we used the set of DEGs defined as padj<0.05,
328 and for the models from Bangash et al, we used the sets of top 300 genes, sorted by pvalue. GSEA
329 analysis for the six models was performed as described for our MM transcriptomic data but ranking
330 the genes by -log(pvalue)*(logFC/abs(logFC). For comparing GSEA results, we selected top 40 most
331 enriched terms in the mouse MM model, sorted by absolute normalized enrichment score, and then
332 extracted the values of the respective terms within the enrichment results corresponding to the other
333 models.
334 *Human transcriptomics sequencing and analyses*

335 Human DRGs were collected from consenting cancer patients under ethical approval from UT Dallas
336 (UTD) and MD Anderson Cancer Centre Institutional Review Boards. Tissue was extracted during
337 thoracic vertebrectomy in patients presenting malignant spinal tumours; sequencing data from these
338 patients has been previously published by Ray PR et al., where the demographic and clinical
339 characteristics of the cohort are described (Ray et al., 2022). Briefly, DRGs were extracted during
340 spinal nerve root ligation and immediately transferred to cold sterile solution, cleaned and stored in
341 dry ice until sequencing. RNA was extracted using TRIzol™ and cDNA was generated using an
342 Illumina Tru-seq library preparation. Sequenced reads were then trimmed and same-length libraries
343 (38bp) mapped to the GENCODE reference transcriptome (Frankish et al., 2019), as previously
344 described (Ray et al., 2022). Data were obtained from two DRGs belonging to one MM patient and
345 68 DRGs obtained from 39 patients; further information is compiled in Supplementary file S2. To
346 evaluate gene expression profiles consistent with MM cell infiltration to the DRG, we first created a
347 custom-made marker set from publicly available data. For this, we combined three high throughput
348 datasets of MM cell gene expression based on different technologies: Affymetrix (Barwick et al.,
349 2021), bulk RNA-Seq (Zhan et al., 2006) and single cell RNA-Seq (Jang et al., 2019), and one dataset
350 measuring expression in normal human DRGs (Ray et al., 2018). For the Affymetrix (Barwick et al.,
351 2021) dataset, we obtained the processed data from the GEO NCBI portal using the GeoQuery R
352 package (v.2.60.0) (Davis and Meltzer, 2007). We mapped the probesets of the HGU133Plus2 chip
353 to Ensembl genes using the custom annotation provided by BrainArray (Dai et al., 2005). The file
354 mapping probesets to Ensembl genes was obtained from the BrainArray download page, version 25
355 (brainarray.mbni.med.umich.edu). Probesets mapping to multiple genes were excluded and when
356 multiple probesets corresponded to the same gene, the one with the highest mean average signal was
357 selected. Probeset intensities were averaged across the 559 replicates, and in total, 16,554 Ensembl
358 genes (of which 15,994 having the biotype "protein coding genes") were uniquely mapped to
359 probesets on the chip. We assigned ranks to genes by sorting them by decreasing average signal
360 intensity. For the RNA-Seq dataset (Zhan et al., 2006), we used the supplementary table with FPKM

361 counts provided in the Gene Expression Omnibus (GEO) platform (study accession number
362 GSE167968). We averaged expression levels across the 33 replicates and ranked genes by decreasing
363 average FPKM units. For the single cell dataset (Jang et al., 2019), we used the supplementary file
364 with transcripts per million (TPM) counts provided in GEO (GSE118900), and counted the number
365 of cells (out of a total 597) in which each gene has a non-zero expression level. Normal DRG
366 expression levels (Ray et al., 2018) were ranked by the decreasing average TPM counts across the
367 three normal tissue samples. Combining the three MM transcriptomic datasets, we obtained a set of
368 2528 genes generally expressed in MM cells, i.e. ranked within the top 10,000 genes in both
369 Affymetrix and bulk RNA-Seq and detected in at least 200 of the 597 cells of the single cell
370 experiment. We further reduced this set to a subset of 40 genes by selecting those with an expression
371 rank >15,000 (corresponding to <0.75 TPM) in normal DRG tissue.

372 We next interrogated MM cell infiltration in human DRG using the MM^{D24} mouse transcriptomic
373 signature as a proxy. For this, we selected the set of upregulated DEGs with a p-adjusted <0.05 in
374 MM^{D24} vs. $sham^{D24}$ mice and evaluated the behavior of their human orthologs in the DRG of MM
375 patients compared to DRGs from patients with other cancer types. For each of the selected
376 markers/DEGs, and for each cancer sample, we computed the percentile expression in relation to the
377 other cancer samples.

378 *Experimental design and statistical analysis*

379 With exception of the transcriptomics experiments (see above), data were analysed and plotted using
380 Graphpad Prism v.9.3.1 (GraphPad Inc., La Jolla, CA, USA), or SAS 9.4 (SAS Institute, Inc., Cary,
381 NC, USA) and are presented as mean ± standard error of the mean (SEM). Group size was determined
382 in G*Power v3.1.9.7 based on our previously published data (Diaz-delCastillo et al., 2020b) to detect
383 a significant difference in limb use on post-surgical day 25 with a 90% power (α error prob. 0.05).
384 Parametric data were analysed by t-test, one-way ANOVA or repeated measures 2-way ANOVA with
385 Tukey´s correction for multiple comparisons, as required. Non-parametric data was analysed by

386 Friedman´s two-way test followed by Wilcoxon´s two-sample test for individual time-points.
387 Transcriptomics data are available in supplementary data or publicly available in GEO (GSE216802);
388 all other data are available upon request.

389

390 **Results**

391 *Intrafemoral inoculation of 5TGM1-GFP cells induces nociception*

392 To understand the time course of neuronal changes leading to MIBP and the mechanisms involved,
393 we conducted a time course study where C57BL/KaLwRijHsd mice were transplanted with 5TGM1-
394 GFP MM cells or vehicle into the medullary cavity of the femur and their pain-like behaviours were
395 assayed over time (Figure 1A). A subset of animals was then euthanized on post-surgical day 17
396 ($sham^{D17}$ and MM^{D17}), prior to development of pain-like behaviours (Figure 1B, C) and another on
397 post-surgical day 24 ($sham^{D24}$ and MM^{D24}), upon the onset of nociception, as measured by the limb
398 use and burrowing tests (Figure 1D, 1E). The choice of non-stimulus evoked behavioural test was
399 informed by our previous model characterization, where we have demonstrated that this model is not
400 sensitive to mechanical or heat hyperalgesia (Diaz-delCastillo et al., 2019). Locomotor activity test
401 was performed to ensure that the observed behavioural deficits were not a result of impaired motor
402 function (Supplementary Fig S1). Disease development was confirmed by paraproteinemia in both
403 animal cohorts (Figure 1G, I). MM^{D24} mice, but not MM^{D17} mice, also presented splenomegaly
404 (Figure 1F, H), a common feature of 5T MM animal models.

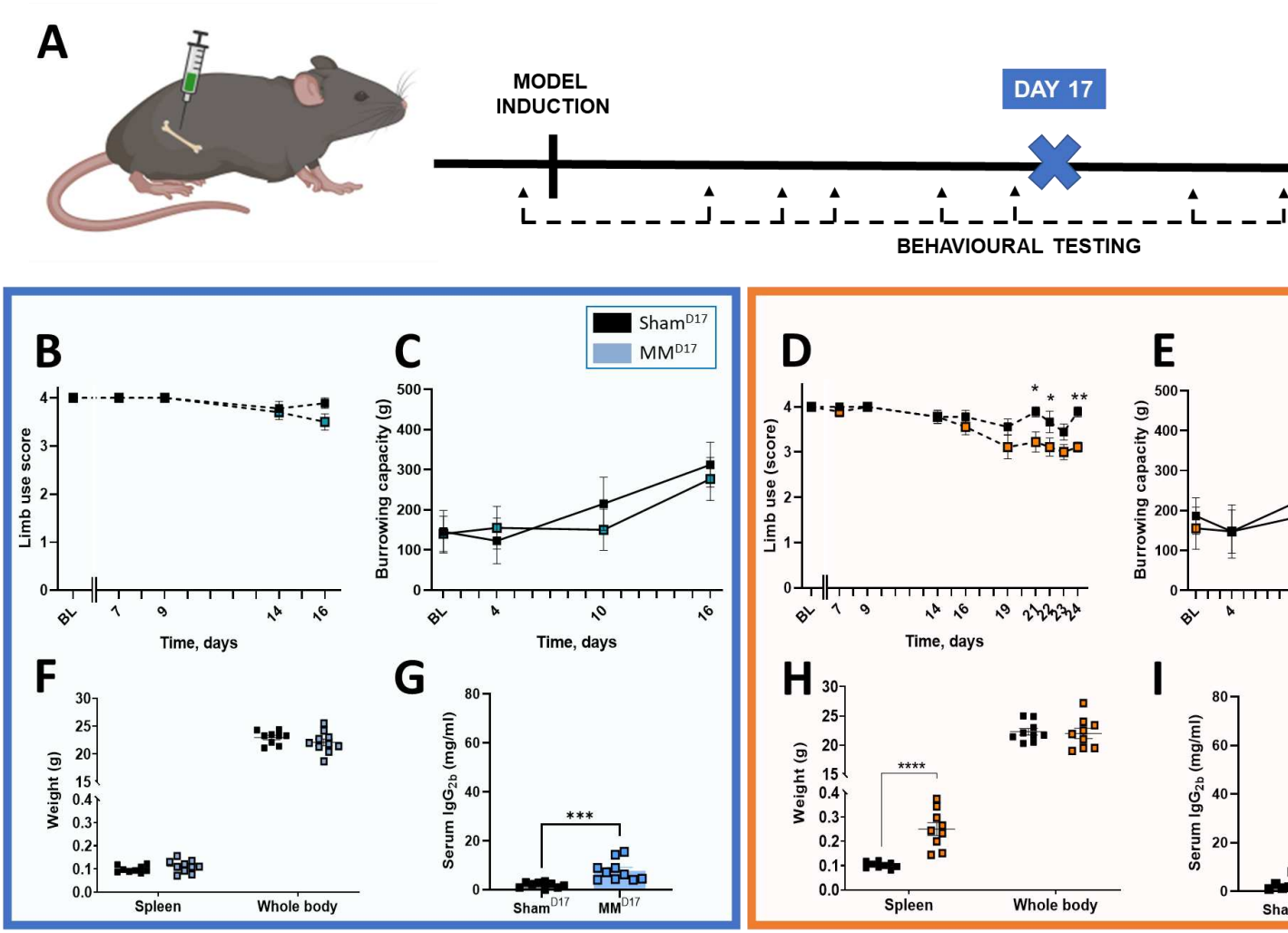

Figure 1. Intrafemoral 5TGM1-GFP cell inoculation in C57BL/KaLwRijHsd mice induces MM disease and pain-like behaviours over time. (A) C57BL/KaLwRijHsd mice were intrafemorally inoculated with 5TMG1-GFP cells or vehicle, their pain-like behaviours were assessed over time, and mice were euthanized on post-surgical day 17 or 24. (B, D) Limb use scores were measured over time. F(1, 180) = 2.10, p=0.0226. Day 21: p=0.0167, Day 22 p=0.0369; Day 24 p=0.0029 by Friedman´s two-way test followed by Wilcoxon´s two-sample test; (C, E) Burrowing capacity measured over time. (F, H) End-point spleen and whole-body weight. t(14)=5.98, p<0.0001 by unpaired, two-tailed Student´s *t*-test. (G, I) Endpoint serum levels of IgG_{2b} paraprotein. D17: t(17)=4.068, p=0.0008; D24: t(16)=3.70, p=0.0019 by unpaired, two-tailed Student´s *t*-test. BL= Baseline. Sham n=8-9; MM n=8-10.

5TGM1-GFP cells induce a time-dependent pattern of osteolytic lesion development

417 In previous experiments we observed a partial analgesic effect of bisphosphonates in the localized
418 5TGM1 model (Diaz-delCastillo et al., 2019), suggesting that MIBP may correlate with osteolysis.
419 Similarly, a plethora of clinical studies have shown that, like in animal models, the clinical analgesic
420 effect of bisphosphonates in MIBP is unclear (Mhaskar et al., 2017). To examine whether the pattern
421 of myeloma-induced osteolysis correlates with the onset of nociception in this model, we performed
422 µCT analyses of the ipsilateral femoral metaphysis of sham and myeloma-bearing bones. We
423 observed that MM^{D24} present a significant increase in cortical lesion area/bone surface (BS),
424 compared with $sham^{D24}$ (Figure 2I, J). In contrast, the lesion area/BS of MM^{D17} remained unchanged,
425 indicating that osteolytic cortical damage develops concurrently to the onset of nociception (Figure
426 2A, B). Furthermore, our analyses revealed unchanged cortical bone volume in both MM^{D17} and
427 MM^{D24} femurs (Figure 2C, K).
428 Next, we evaluated the effect of 5TGM1 cell inoculation in trabecular bone before and during
429 nociception. Densitometric analyses of MM^{D17} trabecular bone revealed a significant decrease in
430 trabecular thickness (Tb.Th) and number (Tb.N), along with increased trabecular spacing (Tb.S),
431 indicating trabecular bone loss prior to the development of nociception (Figure 2F-H). Moreover,
432 MM^{D17} femurs presented decreased trabecular bone volume per total volume (BV/TV) and increased
433 relative bone surface (BS/BV), compared with $sham^{D17}$ (Figure 2D, E). As expected, MM^{D24} femurs
434 presented a similar pattern of trabecular osteolysis, measured as significantly decreased BV/TV and
435 Tb.N., along with increased Tb.Sp (Figure 2 L-P).

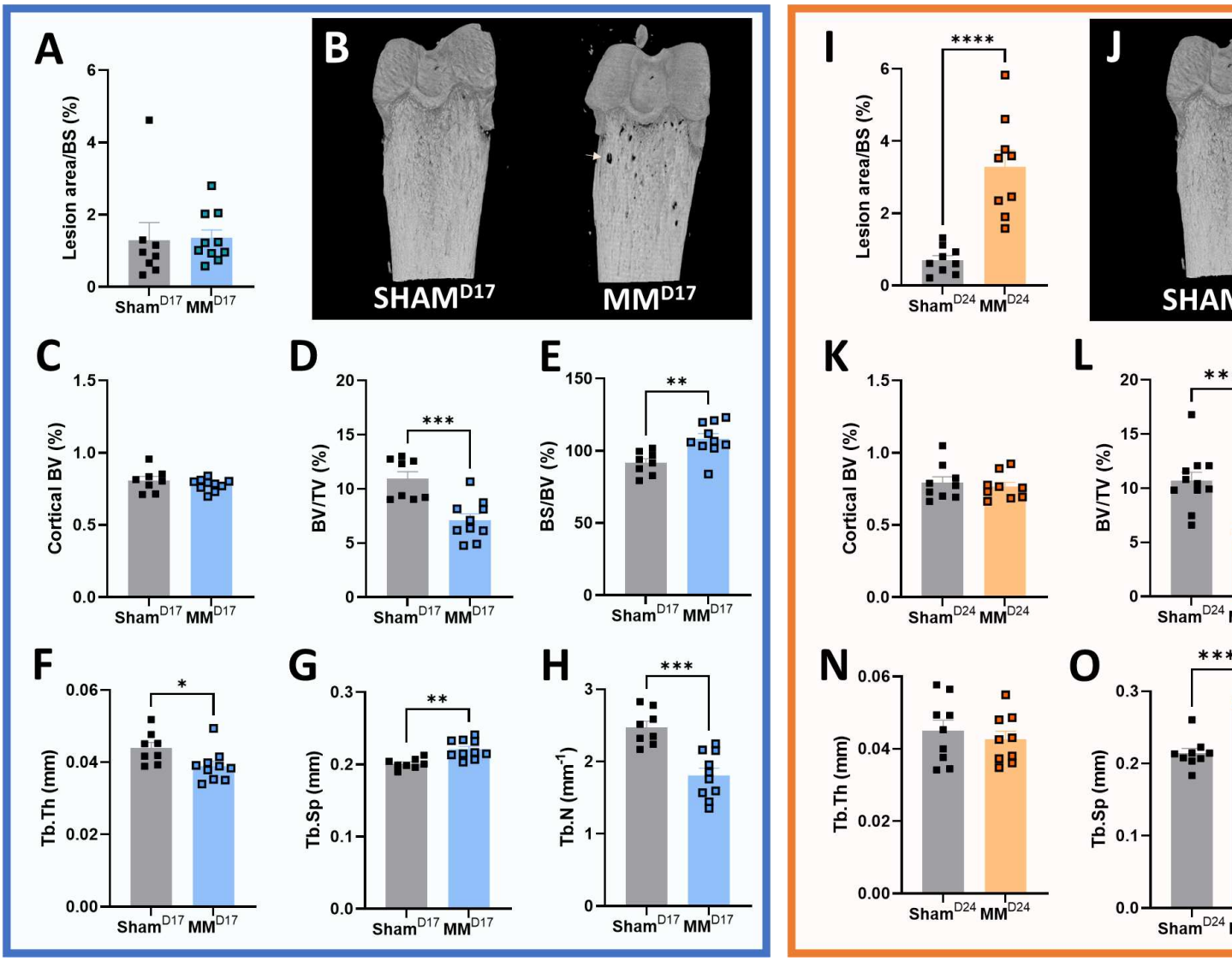

Figure 2. Temporal evolution of myeloma-induced bone disease in 5TGM1-GFP bearing femurs. (A, I) Percentage of lesion area per bone surface (lesion area/BS). t(16)=5.472, p<0.0001 by unpaired, two-tailed Student´s t-test. (B, J) Representative µCT reconstruction images of sham and MM femurs at different time-points; arrows indicate osteolysis. (C, K) Percentage of cortical bone volume (BV). (D, L) Percentage of trabecular bone volume per total volume (BV/TV). Day 17: t(16)=4.323, p=0.0005; Day 24 t(20)=4.107, p=0.0005 by unpaired, two-tailed Student´s t-test. (E, M) Percentage of trabecular bone surface per bone volume (BS/BV). t(16)=3.417, p=0.0035 by unpaired, two-tailed Student´s *t*-test. (F, N) Percentage of trabecular thickness (Tb.Th). t(16)=2.411, p=0.0283 by unpaired, two-tailed Student´s t-test. (G, O) Percentage of trabecular separation (Tb.Sp). Day 17 t(16)=3.903, p=0.0013; Day 24 t(16)=6.381, p<0.0001 by unpaired, two-tailed Student´s t-

447 test. (H, P) Percentage of trabecular number (Tb.N). Day 17 t(16)=4.870, p=0.0002; Day 24
448 t(16)=5.228, p<0.0001 by unpaired, two-tailed Student´s t-test. Sham n=8-9; MM n=9-10.

449 *Multiple myeloma induces periosteal nerve sprouting concomitant to nociception*

450 Our previous studies revealed that 5TGM1 inoculation induced complete bone marrow denervation
451 at the end stages of the model, leading us to speculate that tumour-induced nerve injury contributes
452 to MIBP. To further evaluate the temporal effect of 5TGM1 cell inoculation on the bone marrow
453 microenvironment, we performed immunohistological analyses of sensory (calcitonin-gene related
454 peptide, $CGRP^+$) and sympathetic (tyrosine hydroxylase, TH^+) nerve fibres. We observed that already
455 in MM^{D17} femurs, TH^+ and $CGRP^+$ fibres were not detectable in the bone marrow, which had been
456 colonized by 5TGM1-GFP^+ cells (Figure 3E, G), suggesting that tumour-induced nerve injury
457 precedes the development of MIBP. To confirm that the absence of marrow innervation was not a
458 result of technical difficulties, we identified both TH^+ and $CGRP^+$ nerve fibres in bones of the $sham^{D17}$
459 mice (Figure 3B-D) and in the periosteum of $sham^{D17}$ (Fig 3A, C) and MM^{D17} (F, H).

460 We next sought to examine the effect of intrafemoral 5TGM1-GFP inoculation on periosteal
461 innervation. The periosteum is the bone compartment with the highest nerve density (Mach et al.,
462 2002; Chartier et al., 2018) and alterations to periosteal nerve fibre innervation have been described
463 as a feature of bone pain (Martin et al., 2007; Mantyh, 2014), including cancer-induced bone pain
464 (Mantyh et al., 2010; Bloom et al., 2011). Our analyses revealed infiltration of MM cells to the
465 femoral periosteum of MM^{D24}, which were not present in MM^{D17} femurs. Importantly, we found a
466 significant increase in the density of $CGRP^+$ fibres innervating the periosteum of MM^{D24} mice at the
467 onset of nociception, compared with $sham^{D24}$ (Figure 3I, M, O), which was not present at earlier
468 stages (Figure 3K, O). Similarly, the growth associated protein-43 (GAP-34) marker of axonal growth
469 and regeneration demonstrated significant periosteal sprouting in the later stage of MM development
470 (Figure 3J, L, N, P). Altogether, our data suggests that MM cells induce cortical osteolytic lesions
471 that allow escape to the periosteum, where they may promote periosteal nerve sprouting and
472 contribute to the development of nociception. This was further supported by the significant inverse

473 correlation between periosteal CGRP$^+$ and GAP43$^+$ periosteal nerve sprouting and burrowing
474 capacity (Figure 3Q, R).
475 To investigate the human relevance of our findings, we next performed an explorative study to
476 evaluate whether periosteal infiltration of MM cells in patients is associated with nerve sprouting. In
477 formalin-fixed, paraffin-embedded trephine iliac crest bone biopsies from 13 newly diagnosed MM
478 (NDMM) patients, we performed a multiplex immunostaining for CD138$^+$ MM cells, CD34$^+$ blood
479 vessels and the pan-neuronal marker PGP9.5 (Figure 3S). Our quantification showed that the median
480 periosteal nerve density in NDMM patients was 3.736 profiles/mm^2, ranging from 0 to 82.869
481 profiles/mm^2 (Figure 3T); this is in contrast with reports of periosteal nerve density in non-cancerous
482 patients showing a median of 0.077 profiles/mm^2 (range: 0.02-0.68 profiles/mm^2) (Sayilekshmy et
483 al., 2019). Moreover, we found a significant increase in periosteal nerve density in NDMM displaying
484 periosteal infiltration of CD138$^+$ cells compared with patients without CD138$^+$ cells in the periosteum
485 (Fig 3U), suggesting a direct role for MM cells in promoting nerve sprouting. Periosteal nerve density
486 in NDMM patients was positively correlated with age (Figure 3V) but independent of tumour burden,
487 which was assessed as percentage bone marrow clonality (Figure 3W) and paraproteinemia (Figure
488 3X). Moreover, periosteal nerve density was independent of sex and IgG type (data not shown). This
489 is, to our knowledge, the first evidence of MM-induced alterations to bone innervation in MM patients
490 and altogether our data suggest that periosteal nerve sprouting may play a role in MIBP.

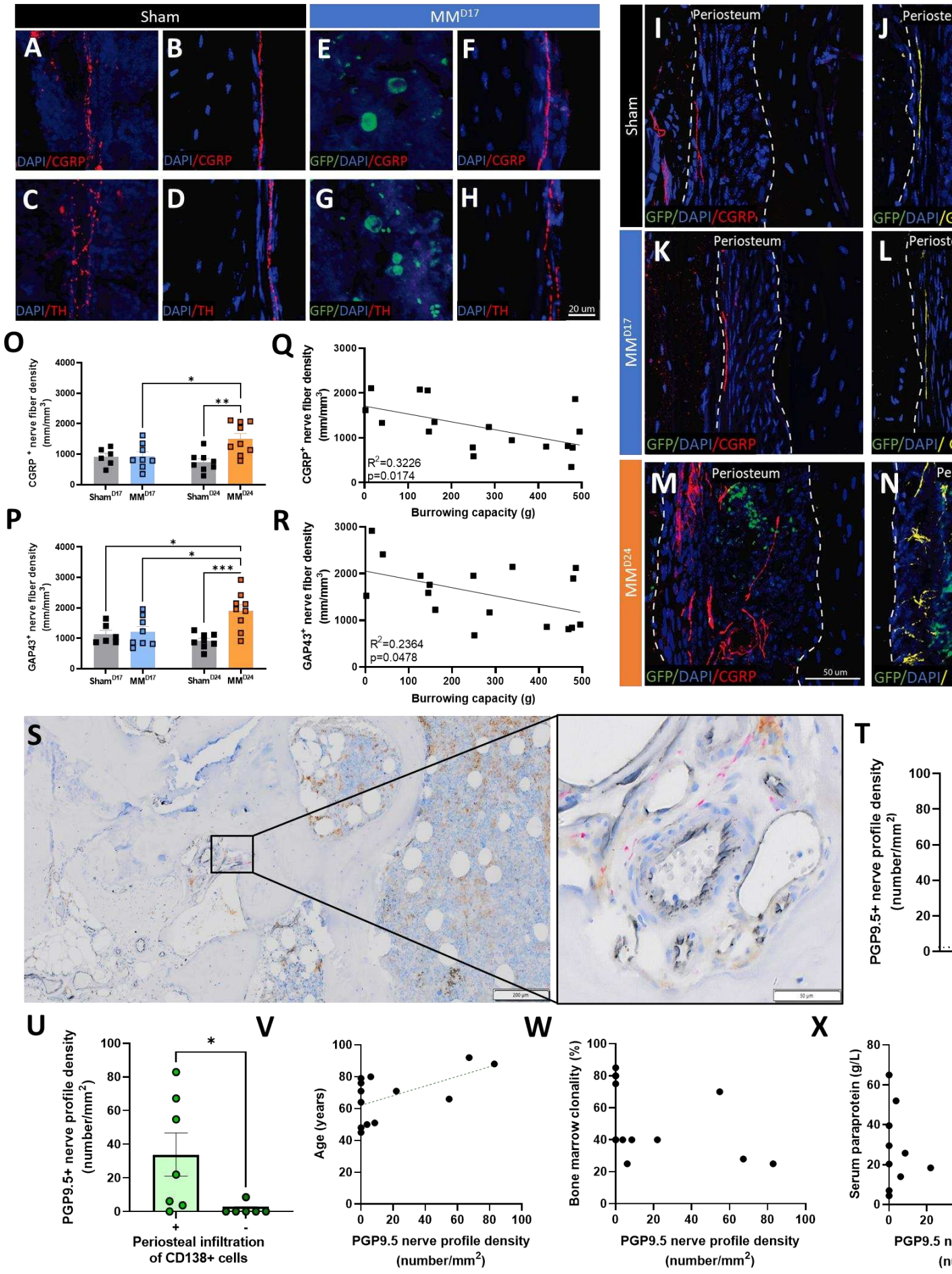
Sham
MMD17
A
B
E
F
DAPI/CGRP
DAPI/CGRP
GFP/DAPI/CGRP
DAPI/CGRP
C
D
G
H
DAPI/TH
DAPI/TH
GFP/DAPI/TH
DAPI/TH
20 um
O
CGRP+ nerve fiber density (mm/mm3)
Sham D17
MM D17
Sham D24
MM D24
Q
CGRP+ nerve fiber density (mm/mm3)
R2=0.3226
p=0.0174
Burrowing capacity (g)
P
GAP43+ nerve fiber density (mm/mm3)
R
GAP43+ nerve fiber density (mm/mm3)
R2=0.2364
p=0.0478
Burrowing capacity (g)
Sham
MMD17
MMD24
I
J
K
L
M
N
Periosteum
GFP/DAPI/CGRP
50 um
S
T
PGP9.5+ nerve profile density (number/mm2)
U
PGP9.5+ nerve profile density (number/mm2)
Periosteal infiltration of CD138+ cells
V
Age (years)
PGP9.5 nerve profile density (number/mm2)
W
Bone marrow clonality (%)
PGP9.5 nerve profile density (number/mm2)
X
Serum paraprotein (g/L)

491

492

493 **Figure 3. MM induces periosteal nerve sprouting in mouse and human tissue.** (A-D)
494 Representative images of $CGRP^+$ (A, B) and TH^+ (C, D) nerve fibres in the bone marrow (A, C) and
495 periosteum (B, D) of sham mice. (E-H) $CGRP^+$ (E) and TH^+ (G) immunoreactivity is undetectable in
496 the bone marrow of MM^{D17}, but visible in the periosteal compartment (F, H). (I-N) Representative
497 images of $CGRP^+$ (I, K, M) and $GAP43^+$ (J, L, N) nerve fibres in the periosteum of $sham^{D24}$ (I, J) and
498 MM^{D24} (M, N). (O) Quantification of relative $CGRP^+$ nerve fiber density. F(1,27)=6.343, p= 0.0180;
499 $sham^{D24}$ vs MM^{D24} p=0.0033; MM^{D17} vs MM^{D24} p=0.0354, $sham^{D17}$ vs MM^{D24} p=0.0470 by two-
500 way ANOVA with Tukey´s correction. (R, S) Quantification of relative $GAP43^+$ nerve density. F(1,
501 27)=7.466, p=0.0110; $sham^{D24}$ vs MM^{D24} p=0.0007; MM^{D17} vs MM^{D24} p=0.0206; $sham^{D17}$ vs MM^{D24}
502 p=0.0162 by two-way ANOVA with Tukey´s correction. (Q, R) Correlation between periosteal
503 sprouting and burrowing capacity. $CGRP^+$ sprouting: R^2=0.3226, p=0.0174 and $GAP43^+$ sprouting:
504 R^2=0.2364, p=0.0478 by two-tailed Pearson correlation. (S) Cross-sections of 3.5-µm trephine iliac
505 crest bone biopsies from NDMM patients were triple stained for $CD138^+$, $CD34^+$ $PGP9.5^+$. (T)
506 Quantification of $PGP9.5^+$ nerve fibres in the periosteum of NDMM patients; dotted line displays the
507 previously reported human periosteal $PGP9.5^+$ nerve density (Sayilekshmy et al., 2019). (U)
508 Periosteal $PGP9.5^+$ nerve density in NDMM patients with or without $CD138^+$ cell infiltration to the
509 periosteum. t(11)=2.312, p=0.0412 by unpaired, two-tailed Student´s *t*-test. (X-Z) Correlation of
510 $PGP9.5^+$ nerve density to age in NDMM. R^2=0.3305, p=0.0398 by two-tailed Pearson correlation. (X,
511 Z) Lack of correlation between periosteal nerve density and tumour burden measured as bone marrow
512 clonality (Y) or serum paraprotein levels (Z). NDMM= Newly diagnosed multiple myeloma. Sham
513 n= 6-8; MM n=8-9. NDMM n=13.

514

515 *Pharmacological blockade of periosteal nerve sprouting induces a transient anti-nociceptive effect*
516 Next, we tested the mechanistic role of periosteal nerve sprouting on MIBP using a therapeutic anti-
517 netrin-1 blocking antibody (NP137). Netrin-1 is an axon guidance molecule known to play a pivotal

518 role in neurogenesis through binding to its canonical receptors UNC5 homolog (UNC5H) and deleted
519 in colorectal cancer (DCC) (Madison et al., 2000; Dun and Parkinson, 2017; Boyer and Gupton,
520 2018). Previous studies have demonstrated a role of netrin-1 on sensory nerve sprouting (Zhu et al.,
521 2019); moreover, silencing netrin-1 reduces hyperalgesia and CGRP+ nerve fiber sprouting in a rat
522 model of disc degeneration (Zheng et al., 2023) and pharmacological netrin-1 inhibition with the NP-
523 137 anti-netrin-1 antibody reduced hyperalgesia in an arthritis model (Rudjito et al., 2021). To
524 investigate whether blockade of periosteal nerve sprouting attenuated MIBP, 5TGM1-GFP inoculated
525 mice were systemically treated with vehicle (MM^{VEH}) or NP137 (MM^{NP137}; 10 mg/kg, i.p). Biweekly
526 treatment with the anti-netrin-1 antibody did not have an overall behavioural effect, but it delayed the
527 onset of nociception, inducing a significant improvement in limb use scores in MM^{NP137} on day 26,
528 compared with MM^{VEH} (Figure 4A). Moreover, NP137 treatment did not affect overall survival
529 (Figure 4B) nor overall tumour burden, as assessed by terminal splenomegaly (Figure 4C). To
530 evaluate whether the transient analgesic effect was a consequence of decreased osteolysis, we
531 performed μCT analyses of endpoint MM^{VEH} and MM^{NP137} femurs. Our results demonstrated that
532 netrin-1 blockage does not affect BV/TV in MM mice (Figure 4D). Moreover, the structural
533 parameters of trabecular bone and bone mineral density were unchanged (data not shown). To confirm
534 the capacity of NP137 treatment to block periosteal nerve sprouting, we next assessed the presence
535 of $CGRP^+$ nerve fibres in the femoral periosteum and found a significant reduction in $CGRP^+$
536 periosteal nerve density in MM^{NP137}, compared with MM^{VEH} (Figure 4E-G). Anatomical presence of
537 a microneuroma was observed in 25% of the vehicle-treated MM mice, (Figure 4G), a feature of the
538 disease never before described but that is consistent with animal models of solid bone cancers such
539 as prostate (Jimenez-Andrade et al., 2010) and breast (Bloom et al., 2011) bone metastases or
540 osteosarcoma (Ghilardi et al., 2010; Mantyh et al., 2010). No microneuromas were observed in
541 MM^{NP137} mice. Systemic antibody treatment by itself in sham mice had no effect on behaviour, bone
542 structural parameters or neuronal innervation (data not shown), and pharmacokinetic analyses
543 confirmed the presence of NP137 in the serum of all treated mice (Supplementary Figure S2).

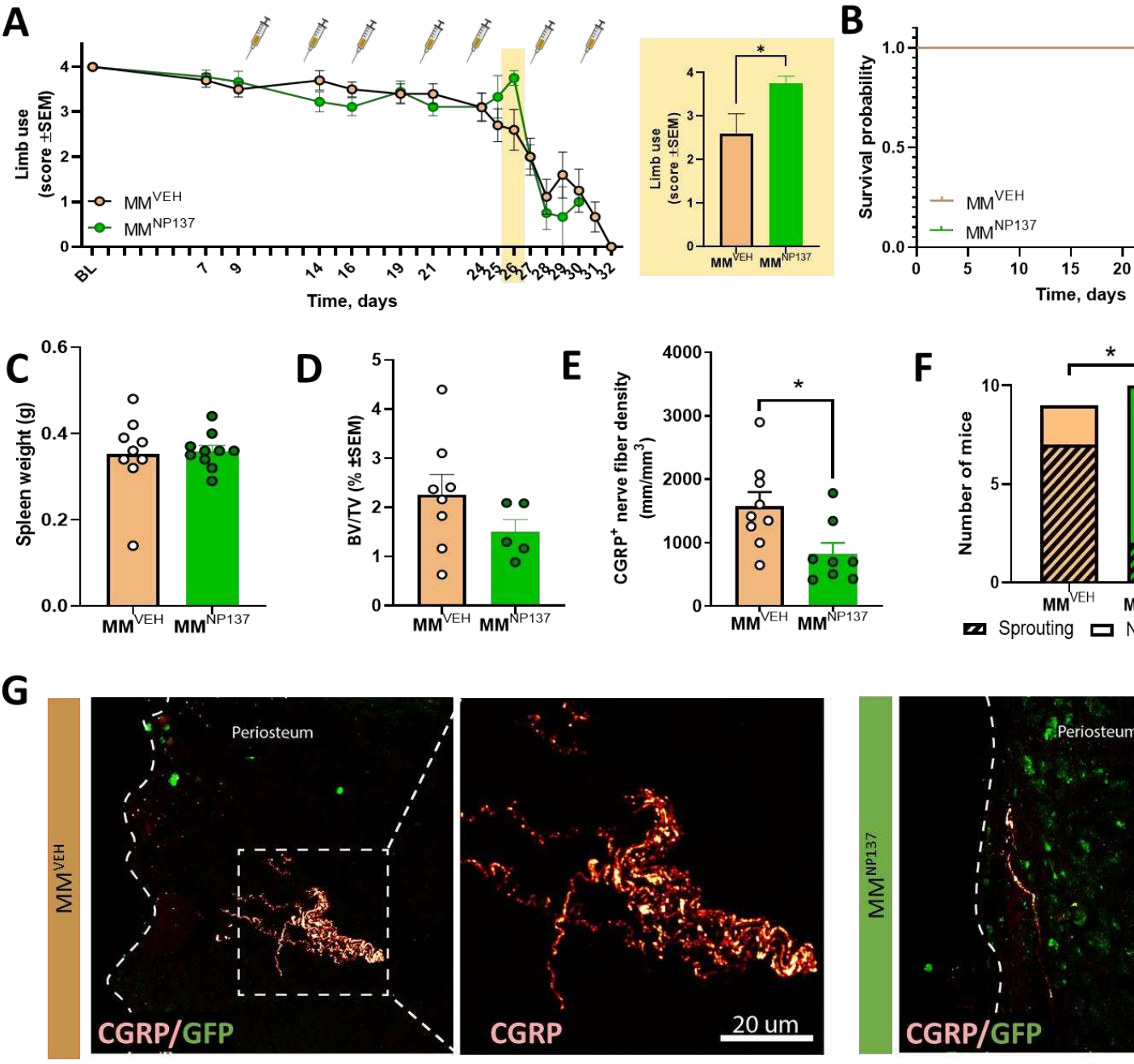

Figure 4. Pharmacological blockage of periosteal nerve sprouting induces a transient anti-nociceptive effect in 5TGM1-bearing mice. (A) Effect of anti-netrin-1 treatment (NP137 10 mg/kg, i.p.; dosing days represented by syringes) or MM mice; exert indicates limb use scores on post-surgical day 26 (onset of pain-like behaviour). t(16)=2.164, p=0.0451 by unpaired, two-tailed student´s t-test. (B) Kaplan-meier curve of vehicle- and NP137- treated MM mice. (C) Endpoint spleen weight. (D) Effect of systemic NP137 treatment on bone osteolysis, measured as bone volume

552 per total volume (BV/TV). (E) Quantification of $CGRP^+$ periosteal nerve density. t(15)=2.63,
553 p=0.0188 by unpaired, two-tailed Student´s t-test. (F) Number of vehicle- or NP137-treated MM mice
554 presenting periosteal nerve sprouting. $Chi^2(1)=6.343$, p=0.0118 by Chi square test. (G)
555 Representative images of periosteal $CGRP^+$ nerve fibres and GFP^+ MM cells in MM mice treated
556 with vehicle or NP137. MM= Multiple myeloma. MM^{VEH} n=9, MM^{NP137} n=10.
557
558 *Dorsal root ganglia (DRG) transcriptomic dysregulation reveals MM infiltration*
559 Following our observation of periosteal sprouting at the onset of nociception, we next hypothesized
560 that MM invasion of the bone niche induces transcriptomic changes in the cell bodies of the
561 innervating nerve fibres. However, considering that blocking of the nerve fibre sprouting only had a
562 transient analgesic effect, there are clearly other mechanisms involved in MIBP. To test this, the DRG
563 transcriptional signature of sham or 5TGM1-GFP inoculated mice during MIBP was evaluated. As
564 expected, MM^{D24} animals displayed nociception (Figure 5A) and splenomegaly (Figure 5B),
565 confirming disease development. On post-surgical day 24, RNA from lumbar DRGs L2, L3 and L4
566 was extracted and sequenced (if RIN>8), resulting in library sizes of 19-22M reads per sample. The
567 mapping rates to the mouse transcriptome were similar across samples, ranging between 88-92% of
568 all reads. We identified 1.389 differentially expressed genes (DEGs) between MM and sham groups
569 with an FDR<5% (Figure 5C, D). Interestingly, the DRG transcriptomic signature of MM mice was
570 highly heterogeneous across samples; this heterogeneity was not correlated to tumour burden (Figure
571 5D). However, significant changes in the expression pattern of DRG gene expression were driven by
572 the presence and transcriptional level of green fluorescent protein (GFP) (Figure 5D), suggestive of
573 MM infiltration to the DRG. Next, we performed gene set enrichment analyses (GSEA) to better
574 interpret the transcriptional dysregulation by taking into account the entire set of genes expressed in
575 our data and without setting up any arbitrary threshold of statistical significance on differential
576 expression. GSEA for GO BP (Gene Ontology biological process) terms and Reactome pathways
577 indicated that the main dysregulated signaling pathways in MM mice were related to cell cycle,

immune response (activated) and neuronal signaling (suppressed) (Supplementary Figures S3 and S4).

Next, we compared the MIBP transcriptomic signature with that of six other models encompassing different painful conditions, as compiled by Bangash et al. (Bangash et al., 2018). These included (Figure 5E) mouse models of painful lung cancer metastasis to the bone (cancer), partial sciatic nerve ligation (PSL), mechanical joint loading (MJL), chemotherapy induced peripheral neuropathy (Oxaliplatin), chronic muscle pain (CMP) and inflammation (Complete Freund´s Adjuvant, CFA). To identify similarities among different painful conditions, we first examined the overlap between the set of MIBP DEGs, and the top 300 genes with smallest p-values from each of the six conditions. Our analyses indicate that MIBP has most DEGs congruent with the PSL and CFA models, suggesting a neuropathic and an inflammatory component (Figure 5E).

Next, we performed (GSEA) for the 6 models and compared results by selecting the top 40 enriched GO BP terms or Reactome pathways in MIBP and visualizing their normalized enrichment score and corresponding adjusted p-values across all models (Figure 5F and Supplementary Figure 4). Interestingly, the transcriptional signature of MM was overall most similar to that of PSL, suggesting a strong neuropathic component in MIBP. These results are in line with our previous finding of periosteal nerve sprouting as a contributing mechanism to MIBP. Even though the overlap of DEGs is higher with the CFA model, the comparative GSEA analysis indicates that this similarity is only retained at the level of common activated inflammation-related pathways. Since spinal microglial reaction is a well-known feature of neuropathic pain (Chen et al., 2018; Inoue and Tsuda, 2018), we characterized the expression of ionized calcium-binding adaptor molecule 1 (Iba1) and phospho-p38 mitogen-activated protein kinase (P-p38 MAPK) in the dorsal horn of the spinal cord of sham^{D24} and MM^{D24} mice. No changes in relative Iba1^{+} or Pp38^{+} cell number were observed at any lumbar region (Supplementary Figure S5). Likewise, no changes in glial fibrillary acidic protein (GFAP) staining were observed, suggesting that astrocytosis is not a main feature of MIBP (Supplementary Figure S5).

604

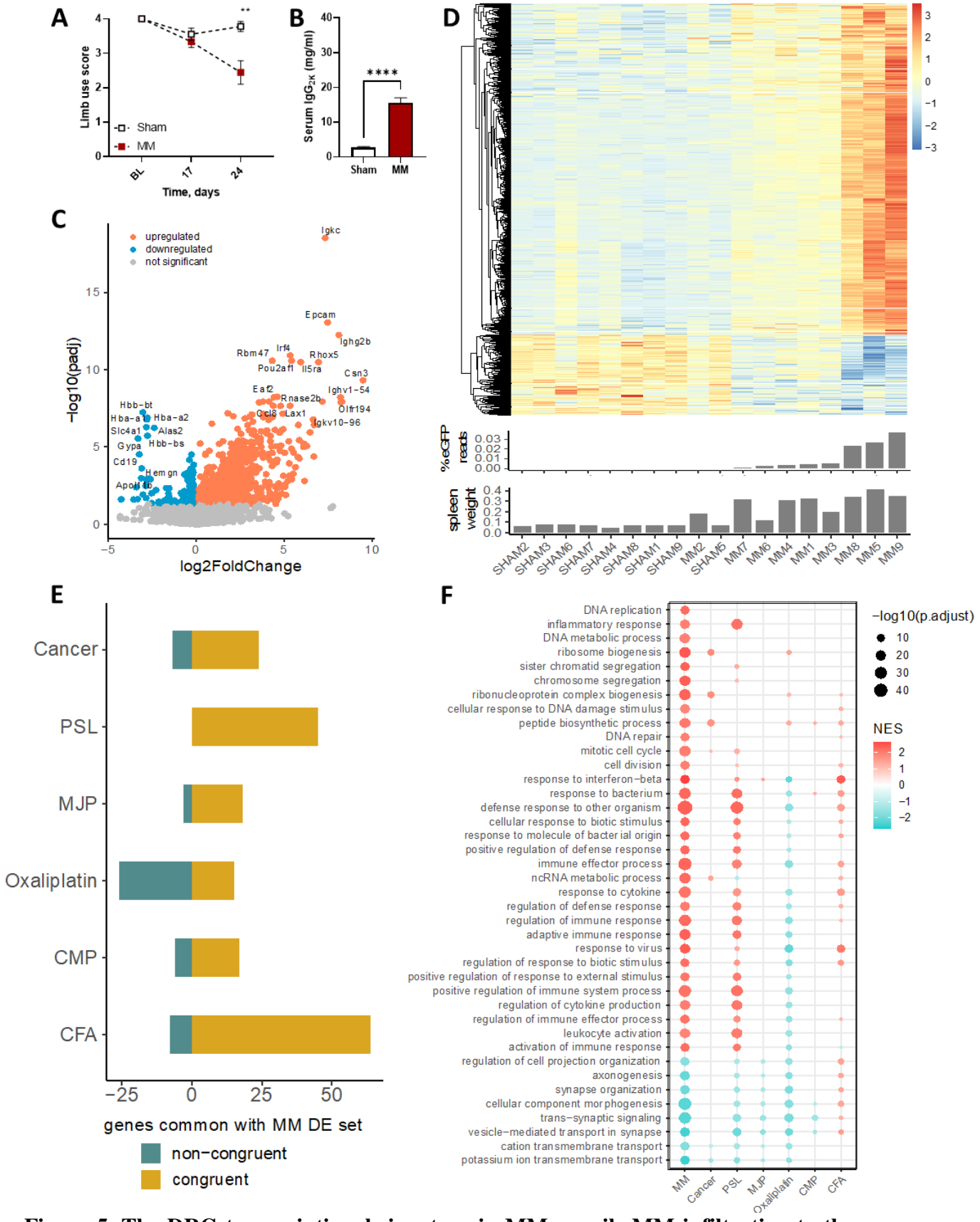

605 **Figure 5. The DRG transcriptional signature in MM unveils MM infiltration to the nervous**

606 **system and a strong neuropathic component.** (A, B) Development of nociception (A) and

607 splenomegaly (B) were confirmed prior to DRG isolation and transcriptomic analyses. F(1, 36) =
608 0.0127; Day 24 p=0.0012 by Friedman´s two-way test followed by Wilcoxon´s two-sample test and
609 t(16)=9.106, p<0.0001 by unpaired, two-tailed Student´s t-test. (C) Volcano plot showing the log2
610 fold change of differentially expressed genes (DEGs) between sham^{D24} and MM^{D24}. (D) Heatmap
611 depicting z-scaled regularized log counts of the 1389 DEGs identified between sham and MM lumbar
612 DRGs (adjusted p-value<0.05). The heterogeneous transcriptome of MM DRG was correlated to the
613 presence and levels of GFP expression. (E) Comparison to other mouse pain models in terms of
614 common DEGs. The overlap between the DEGs identified in MM mice and top 300 DEGs, sorted by
615 p-value, in other painful models, as reported by Bangash et al (Bangash et al., 2018), highlights the
616 neuropathic and inflammatory component of MIBP. In yellow, common DEGs congruent in their
617 direction of regulation between MM and each of the other models; in blue, common DEGs in non-
618 congruent direction of regulation. (F) Model comparison in terms of GSEA. Normalized enrichment
619 scores (NES) and their corresponding p-values for the top 40 enriched GO terms in MIBP are
620 displayed across all seven pain models(Bangash et al., 2018), indicating that the PSL model is the
621 most similar to MIBP. MM= Multiple myeloma. PSL= Partial sciatic nerve ligation. MJP=
622 Mechanical joint loading. CMP= chronic muscle pain. CFA= Complete Freund´s adjuvant. Sham
623 n=9; MM n=9.
624
625 *MM infiltration and increased ATF3 expression in DRGs from MM^{D24} mice.*
626 To further verify that the GFP reads detected during transcriptome sequencing were caused by MM
627 infiltration to the DRG and not the result of sample contamination, we performed immunofluorescent
628 GFP staining on the ipsilateral DRGs of sham and MM bearing mice euthanized on post-surgical day
629 17 or 24 (Figure 6A, B). We found 5TGM1-GFP infiltration in the ipsilateral L2 DRG of all MM^{D24}
630 mice confirming the results from the transcriptomic analysis (Figure 6C). Similar results were found
631 in the ipsilateral L3 (data not shown). No GFP expression was detected in DRGs of MM^{D17} and sham

632 controls (Figure 6B, C). Thus, our data indicate that MM has the capacity to metastasize to the
633 peripheral nervous system, which occurs concomitantly to development of nociception.
634 Next, we examined the integrity of DRG vascularization and potential neuronal damage through
635 immunofluorescent staining of the ipsilateral DRG of sham and MM mice 17 or 24 days after cell
636 inoculation. Our analyses of $CD31^{+}$ blood vessels (Figure 6D) revealed a significant decrease in blood
637 vessel length (Figure 6E-G) and density (Figure 6H-J) in DRGs from MM^{D24}, but not MM^{D17},
638 compared with sham at all the analysed lumbar levels. The proportion of sympathetic TH^{+} neurons
639 was similar across samples (Figure 6 L); however, the percentage of activating transcription factor 3
640 $(ATF3)^{+}$ neuron profiles was significantly increased in ipsilateral MM^{D24} as compared to $sham^{D24}$,
641 suggesting tumour-induced neuronal injury (Figure K, M). Additionally, ATF3 and 4′,6-diamidino-
642 2-phenylindole (DAPI) staining revealed a specific pattern of nuclear staining consistent with the
643 development of Nagoette nodules, indicative of neuronal degeneration (Peters et al., 2007) (Figure
644 6K). Finally, we examined the contralateral MM^{D24} DRGs and found intact vasculature and low levels
645 of ATF3 expression (data not shown), suggesting that MM DRG infiltration and concomitant
646 vasculature and neuronal damage may be a specific mechanism of MIBP.

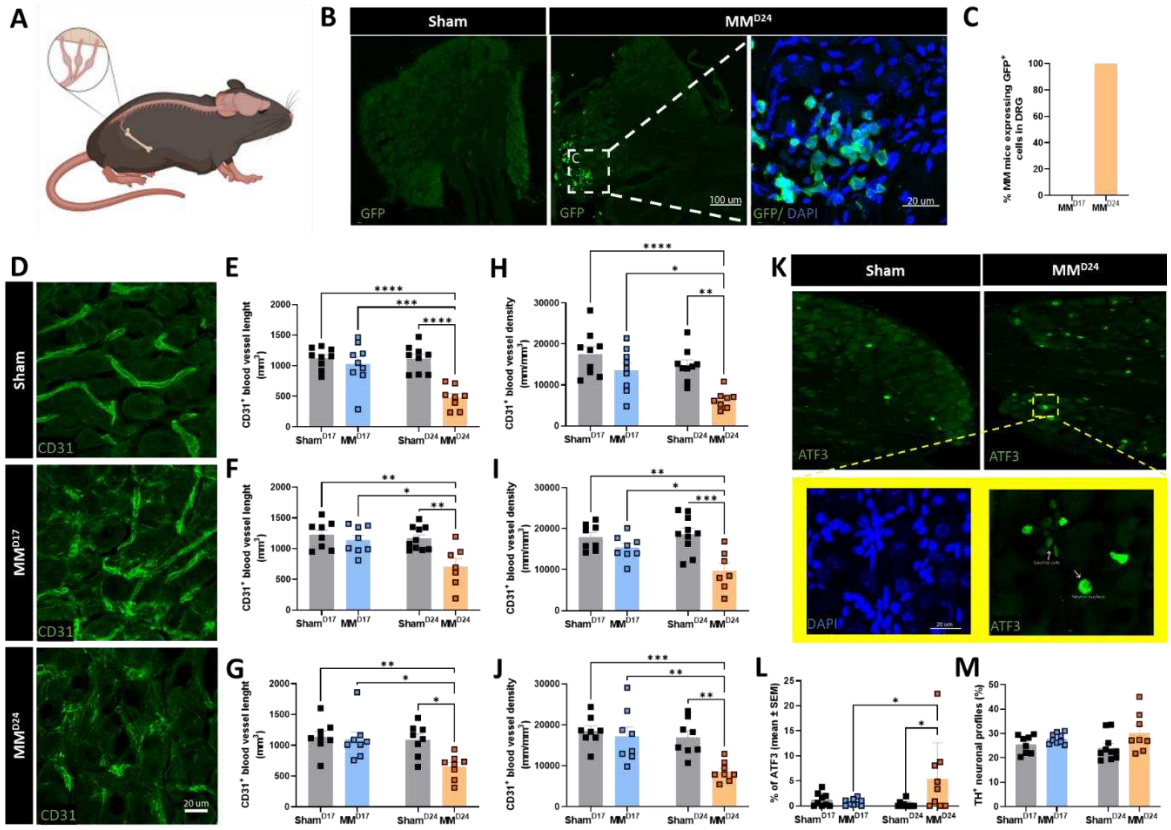

Figure 6. MM cells metastasize to the DRG causing damage to vasculature and neuronal bodies. (A) Ipsilateral and contralateral lumbar DRGs L2, L3 and L4 were collected. (B) Frozen sections from L3 DRGs were immunostained for GFP. (C) Number of MM bearing mice presenting GFP^+ staining in the ipsilateral L3 DRG. (D) Representative images of $CD31^+$ immunostaining in DRG frozen sections. Note the structural injury to $CD31^+$ blood vessels in MM^{D24}, indicated by white arrows. (E, F, G) Quantification of $CD31^+$ blood vessel length in the ipsilateral L2 (E), L3 (F) and L4 (G) DRGs. (E) $F(1,31)=10.57$, $p=0.0028$, $Sham^{D24}$ vs MM^{D24} $p=0.0004$; MM^{D17} vs MM^{D24} $p<0.0001$; $sham^{D17}$ vs MM^{D24} $p<0.0001$; (F) $F(1,29)=4.610$, $p=0.0403$, $Sham^{D24}$ vs MM^{D24} $p=0.0105$; MM^{D17} vs MM^{D24} $p=0.0036$; $sham^{D17}$ vs MM^{D24} $p=0.0017$; (G) $F(1,28)=4.321$, $p=0.0469$, $Sham^{D24}$ vs MM^{D24} $p=0.0129$; MM^{D17} vs MM^{D24} $p=0.0142$; $sham^{D17}$ vs MM^{D24} $p=0.0056$ by two-way ANOVA followed by Tukey´s correction. (H, I, J) Quantification of relative $CD31^+$ blood vessel density in the ipsilateral L2 (H), L3 (I) and L4 (J) DRGs. (H) $F(1,31)=2.214$, $p=0.1468$, $Sham^{D24}$ vs MM^{D24} $p=0.0119$; MM^{D17} vs MM^{D24} $p=0.0028$; $sham^{D17}$ vs MM^{D24} $p<0.0001$; (I) $F(1,29)=5.178$, $p=0.0304$, $Sham^{D24}$ vs MM^{D24}

662 p=0.0499; MM^{D17} vs MM^{D24} p=0.0005; $sham^{D17}$ vs MM^{D24} p=0.0022; (J) F(1,28)=10.31, p=0.0033,
663 $Sham^{D24}$ vs MM^{D24} p=0.0037; MM^{D17} vs MM^{D24} p=0.0051; $sham^{D17}$ vs MM^{D24} p=0.008 by two-way
664 ANOVA followed by Tukey´s post-hoc test. (L) TH^+ quantification in frozen sections from L2 DRGs.
665 (K) $ATF3^+$ immunoreactivity; exert denotes high-resolution imaging of $ATF3^+$ and DAPI
666 immunoreactivity on ipsilateral L2 MM^{D24} DRG. Note the presence of Nagoette nodules denoted with
667 white arrows, suggestive of neuronal degeneration. (M) $ATF3^+$ quantification in L3 DRGs.
668 F(1,33)=5.363, P=0.0269; $Sham^{D24}$ vs MM^{D24} p=0.0492; MM^{D17} vs MM^{D24} p=0.0239 by two-way
669 ANOVA followed by Tukey´s post-hoc test. (O). MM= Multiple myeloma. Sham n=8-9; MM n= 7-
670 10.
671
672
673 *The transcriptomic DRG signature of a MM patient suggests metastatic infiltration*
674 Following our unexpected observation of MM metastasis to the DRG of myeloma-bearing mice
675 displaying MIBP, we questioned the translational validity of our findings. To evaluate whether the
676 genetic signature of MM cells was present in peripheral nervous system of a MM patient, we accessed
677 the transcriptome of 68 DRGs collected from 39 patients with 18 different types of cancer (Ray et al.,
678 2022), as well as that of two thoracic DRGs from one MM patient. Median age of the patient cohort
679 was 60 years (spamming from 33-79 years) and 15 patients were females (35.58%); detailed patient
680 characteristics have previously been reported (Ray et al., 2022). First, we used publicly available
681 datasets to generate a transcriptomic signature of composed of human markers generally expressed
682 in MM cells (Zhan et al., 2006; Jang et al., 2019; Barwick et al., 2021) that show low or no expression
683 in healthy DRG tissue (Ray et al., 2018). Datasets were chosen to represent different high throughput
684 technologies (Affymetrix, bulk RNA-seq and single cell RNA-seq) and the final MM signature
685 contained 40 genes that were ranked within the top 10,000 genes in Affymetrix and bulk-RNA,
686 detected in over a third of single-cell RNA-seq cells, and had an expression rank <0.75 TPM in normal
687 DRG tissue. Gene expression of the 40 signature markers was generally higher in the DRGs of the

688 MM patient compared with most other cancer samples (Figure 7A). Indeed, the distribution of
689 percentile gene expression of the two MM samples over the other cancer samples, across the 40 MM
690 markers, showed a general shift towards higher percentiles (Figure 7B), with a mean percentile of
691 71,6 (mean of the two samples from the MM patient). In order to check whether other cancer samples
692 displayed a similarly high or higher MM signature, we plotted the mean percentile marker distribution
693 for all other 68 cancer samples and confirmed that MM samples showed among the highest mean
694 percentile (Figure 7C). Other samples with a high mean percentile (indicative of similarly enriched
695 expression for the selected marker genes) were DRGs from prostate and renal cell carcinoma patients
696 (Supplementary File S2).
697 Next, we asked if the MIBP transcriptomic signature identified in our animal experiments was
698 translatable to the human condition. Since the DEGs observed in MM^{D24} vs $sham^{D24}$ mice seemed to
699 be largely driven by MM cell infiltration to the DRG, we hypothesized that these DEGs are either
700 expressed in MM cells or disrupted as a result of MM infiltration and could be used as a proxy for
701 MM metastasis in patient data. Thus, we selected the set of human orthologs to the mouse upregulated
702 DEGs (padj<0.05) in MM^{D24}, resulting in a set of 797 genes. Like with the human datasets, the
703 relative gene expression of the chosen markers displayed a distribution shift towards higher
704 percentiles, indicating a tendency towards overexpression of the genes from this set in the human
705 MM DRGs compared to other cancers (Figure 7D). The MM samples showed among the highest
706 mean percentile (mean of the two MM samples - 66,4) (Figure 7E). Taken altogether, our data suggest
707 that cancer metastasis to the DRG may also occur in MM patients.

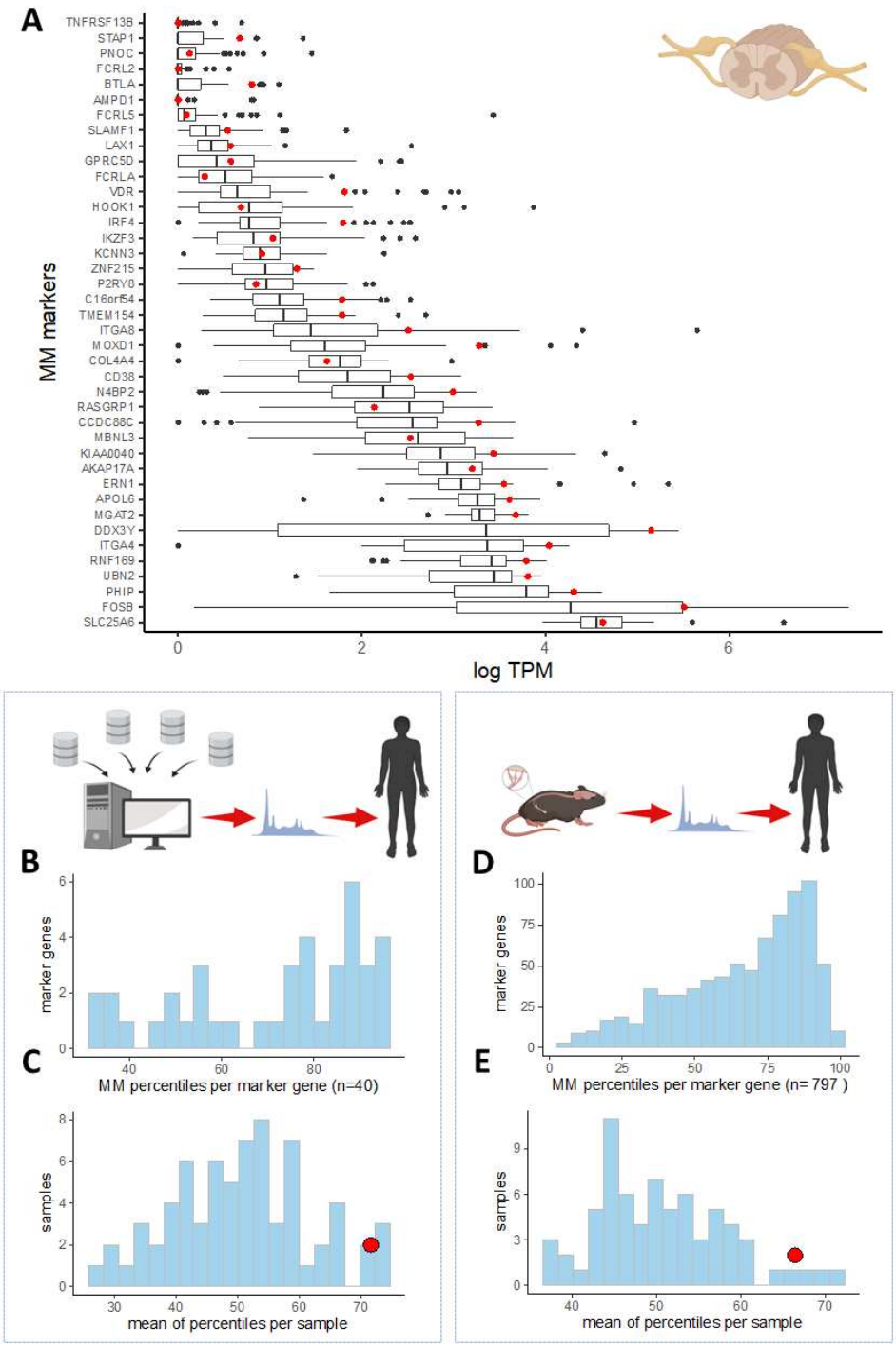

Figure 7. The transcriptomic signature of a MM patient suggest cancer infiltration to the DRG. (A) Box-plot of log FPKM counts for the 40 signature MM markers across 70 DRGs from cancer patients. Red dots indicate the mean expression level in two thoracic DRGs from one MM patient. (B) Distribution of percentile gene expression for all 40 markers in the DRGs of the MM patient. (C) Distribution of mean percentiles across all cancer samples; red dot indicates the mean percentile for the MM patient. (D) Distribution of percentile gene expression for the signature set derived from the mouse MM^{D24} upregulated DEGs (padj<0.05). (E) Distribution of mean percentiles across all cancer

716 samples; red dot indicating the mean percentile for the MM patient, for the mouse MM^{D24} derived
717 set.
718

719 **Discussion**

720 Bone pain remains among the main complaints from MM patients and significantly impairs their
721 quality of life; indeed, previous reports have highlighted that MM patients report more symptoms and
722 problems than leukaemia and lymphoma patients (Johnsen et al., 2009). However, the preclinical
723 search for adequate analgesic options for MIBP is scarce and pathophysiological mechanisms
724 underlying bone cancer pain are poorly understood (Hiasa et al., 2017; Olechnowicz et al., 2019;
725 Diaz-delCastillo et al., 2020b).

726 In this study, we use our previously characterized local immunocompetent mouse model of MIBP
727 (Diaz-delCastillo et al., 2020b) to investigate disease-driven alterations of the central and peripheral
728 nervous system that may lead to rational search of new analgesic targets. Following 5TGM1-GFP
729 cell transplantation into the intrafemoral marrow of a tumour-permissive mouse strain, we observed
730 the progressive development of non-stimulus evoked nociceptive behaviours that can be considered
731 as surrogate markers of spontaneous pain and/or wellbeing (Deacon, 2006; Sliepen et al., 2019).
732 Behavioural tests and experimental time-points (i.e. collection of tissue on post-surgical day 17 or
733 24) were selected according to our previous model characterization (Diaz-delCastillo et al., 2019).
734 Indeed, we have previously shown that systemic opioid administration (10 mg/kg morphine) on post-
735 surgical day 26 reverses the MM induced deficits in limb use, further confirming model validity
736 (Diaz-delCastillo et al., 2019).

737 Following the direct transplantation of 5TGM1-GFP cells into a permissive microenvironment, we
738 observed trabecular bone loss as early as post-surgical day 17, prior to the development of
739 nociception. This apparent disconnection between osteolytic damage and nociception is consistent
740 with preclinical and clinical evidence highlighting the limited analgesic efficacy of commonly used
741 anti-resorptive treatments such as bisphosphonates (Mhaskar et al., 2017; Porta-Sales et al., 2017;

742 Coluzzi et al., 2019; Diaz-delCastillo et al., 2019). In contrast, we observed cortical osteolysis at later
743 stages of the disease, coinciding with the onset of nociception and suggesting periosteal involvement
744 in MIBP. To confirm this, further immunostaining demonstrated 5TGM1-GFP cell escape to the
745 periosteum of these bones, along with significant sprouting of sensory neurons, concomitant to
746 nociception. Periosteal nerve sprouting has been posed as a potential mechanism of cancer-induced
747 bone pain in animal models of breast (Bloom et al., 2011) and prostate bone metastasis (Jimenez-
748 Andrade et al., 2010), as well as osteosarcoma (Mantyh et al., 2010), and anti-NGF therapy has
749 recently showed modest results for the treatment of cancer pain (Sopata et al., 2015). Our results
750 support the hypothesis that myeloma cells cause osteolytic cortical lesions through which they escape
751 to the periosteum, where they may release neurotrophic factors that promote nerve sprouting and,
752 potentially, nociception. The translational implication of these pre-clinical results is further supported
753 by our exploratory observation of increased periosteal nerve density in NDMM patients compared to
754 patients with hyperparathyroidism (Sayilekshmy et al., 2019), and the observation that periosteal
755 nerve sprouting occurred more frequently in patients with periosteal infiltration of MM cells. Future
756 studies addressing periosteal nerve sprouting in patients with MM and healthy controls are needed to
757 confirm our findings.
758 To evaluate the contribution of periosteal nerve sprouting to MIBP, we tested the effect of repeated
759 systemic NP137 administration. NP137 is a humanized monoclonal antibody targeting Netrin-1 that
760 is currently undergoing Phase I and II clinical trials (NCT02977195; NCT04652076) as an anti-cancer
761 treatment. Because Netrin-1 is a neurotrophic ligand involved in axon guidance, we expected that
762 NP137 treatment would prevent periosteal nerve sprouting and, consequently, MIBP. Our results
763 demonstrated that netrin-1 blockage effectively prevents periosteal nerve sprouting in myeloma-
764 bearing mice without affecting bone morphometry. In contrast to previous studies (Fahed et al., 2022),
765 systemic NP137 administration failed to have an effect of tumour burden or survival. While the
766 reasons for this discrepancy are unknown, serum levels of sham drug-treated mice were twice as high
767 compared to those of MM drug-treated mice, suggesting increased antibody clearance and volume

768 distribution in MM-bearing mice. Future studies with greater doses of this antibody in mice with MM
769 are warranted to determine its effect on tumour and disease progression.
770 Next, we evaluated the transcriptional DRG signature of MIBP and compared it to that of other pain
771 models, including bone cancer metastasis, peripheral neuropathy, inflammation and chemotherapy-
772 induced bone pain, as previously described (Bangash et al., 2018). Our data suggested that the
773 transcriptional signature of MM bone pain was more similar to that of neuropathic and inflammatory
774 pain than to the other pain models. While it has been speculated that central-acting agents targeting
775 sensitization (i.e. gabapentin and antidepressants) may pose an alternative for the management of
776 MIBP (Coluzzi et al., 2019), there is a lack of evidence supporting this treatment line. Detailed
777 examination of the spinal cord in MM and sham mice revealed neither microglia activation not
778 astrocyte reaction in the dorsal horn of the spinal cord at any investigated time-point.. However,
779 central sensitization may occur without astrocytic or glial involvement, and we and others have
780 previously reported that spinal microglial reaction in cancer-induced bone pain models is a highly
781 variable occurrence that may not reflect the clinical reality (Honore et al., 2000; Diaz-delCastillo et
782 al., 2020a). Instead, the neuropathic component of MIBP is in line with clinical reports describing
783 baseline peripheral neuropathy in a proportion of MM patients (Richardson et al., 2012; Oortgiesen
784 et al., 2022), which is also used as a prognostic factor of chemotherapy induced peripheral neuropathy
785 and treatment outcome in this patient population (Dong et al., 2022). These results, in combination
786 with our observation of periosteal nerve sprouting, suggest that medications targeted to neuropathic
787 pain patients may be useful to treat a fraction of myeloma bone pain patients. However, our approach
788 has several limitations, including that the GSEA comparison between our MM model and those
789 described by Bangash et al (Bangash et al., 2018) is directly impacted by the quality of the data from
790 each of the models. Thus, while the PSL model was the most similar to MM, it was also the one
791 showing the highest statistical significance for the DEG analysis and resulted also in a higher number
792 of significant GSEA terms; in contrast, cancer, CMP and MJP models (i.e. those with the lowest

793 degree of similarity to MM) showed no DEGs falling within the threshold after FDR correction for
794 the models, which may hinder the significance of our findings.
795 Among the most important findings from our mouse transcriptomics analyses was the high
796 heterogeneity in the pattern of DEG in MM mice. Interestingly, the MIBP transcriptional signature
797 was not correlated to surrogate markers of tumour burden or nociception but was instead highly
798 dependent on the number of GFP counts. These results strongly suggest MM metastases to the
799 ganglia, a never-before described feature of the disease that we further confirmed through
800 immunohistological staining. Along with the spatial localization of MM cells in the ganglia, we
801 observed structural damage and reductions in length and density of blood vessels innervating the
802 lumbar ganglia. Whether damage to the blood vessels occurs prior to neoplastic infiltration (thus
803 allowing the passage of MM cells into the DRG) or is a consequence of it, remains to be elucidated.
804 In any case, neoplastic infiltration of the ganglia occurs concomitant to neuronal damage, as
805 demonstrated by the increase in $ATF3^{+}$ nerve profiles and the formation of nodules of Nagoette
806 (Peters et al., 2007). This novel observation of neuronal degeneration at the onset of MIBP presents
807 a new research avenue that requires further research to identify potential treatment targets; future
808 studies could address the mechanisms of MM metastasis to the DRG and the involvement of
809 immunomodulators in DRG colonization.
810 Our human transcriptomic analyses revealed a similar indication of possible neoplastic infiltration in
811 the DRGs of a MM patient. To our knowledge, the only previous publication addressing this question
812 is from 1958, when Dickenman et al. (Dickenman and Chason, 1958) found degenerative changes
813 but no cancer infiltration in the DRGs of eight deceased MM patients. In contrast, we have performed
814 bulk sequencing of two thoracic DRGs from a MM patient and compared our transcriptomic results
815 to those of 39 patients with other cancer types. Comparing our custom-made MM transcriptional
816 signature composed by MM genes with low or no expression in healthy DRG as per publicly available
817 datasets to the gene expression profile of all 70 DRGs suggested that MM gene expression was
818 enriched in the DRGs from the MM patient. Similarly, evaluating the expression pattern of human

819 orthologs to DEG identified in MIBP mice revealed enrichment in the MM patient DRGs. This
820 observational data supports the translational validity of our findings with the obvious limitation of
821 the highly restricted sample number. Accessing quality human DRG tissue is challenging, but further
822 research is needed to conclude whether cancer metastasis to the DRG is indeed a common occurrence
823 in MM patients.
824 In conclusion, our data suggests that MIBP is mediated by concomitant mechanisms including
825 periosteal nerve sprouting and neoplastic infiltration of the DRG. Moreover, the transcriptional
826 signature of MIBP indicates a neuropathic component and pain management in MM patients may
827 require a multi-targeted approach that include drugs targeting neuropathic pain.
828

829 **Funding and competing interests**

830 This study has been funded by IMK Almene Fond and Brødrene Hartmanns Fond. Part of the work
831 was funded by the Novo Nordisk Foundation (NNF14CC0001). The funding bodies played no role
832 in data collection, analyses, or interpretation, nor in manuscript preparation. The authors disclose no
833 competing interests.
834

835 **Authors´ contributions**

836 MDC and AMH: study conceptualization, funding acquisition and manuscript preparation. MDC, LJ,
837 MAL, TLA, JMJA and AMH: study design. MDC, TN, DMT, NACS, JAVM, LPG, HE, DN, PMD
838 MAL, JMJA and AMH: mouse experiments and data processing. MDC, OP, LJ and AMH: planning,
839 performing and analysing the transcriptomics mouse experiment. MDC, JC, TJP, PMD, OA:
840 planning, performing and analysing human transcriptomics data. MDC, REA, AM, ADC, TLA and
841 AMH: collection and analyses of human bone biopsies.
842

843 **References**

844 Bangash MA, Alles SRA, Santana-Varela S, Millet Q, Sikandar S, de Clauser L, Ter Heegde F, Habib AM, Pereira
845 V, Sexton JE, Emery EC, Li S, Luiz AP, Erdos J, Gossage SJ, Zhao J, Cox JJ, Wood JN (2018) Distinct

846 transcriptional responses of mouse sensory neurons in models of human chronic pain conditions.
847 Wellcome Open Res 3:78.
848 Barwick BG, Gupta VA, Matulis SM, Patton JC, Powell DR, Gu Y, Jaye DL, Conneely KN, Lin YC, Hofmeister CC,
849 Nooka AK, Keats JJ, Lonial S, Vertino PM, Boise LH (2021) Chromatin Accessibility Identifies
850 Regulatory Elements Predictive of Gene Expression and Disease Outcome in Multiple Myeloma.
851 Clinical cancer research : an official journal of the American Association for Cancer Research 27:3178-
852 3189.
853 Bloom AP, Jimenez-Andrade JM, Taylor RN, Castaneda-Corral G, Kaczmarska MJ, Freeman KT, Coughlin KA,
854 Ghilardi JR, Kuskowski MA, Mantyh PW (2011) Breast cancer-induced bone remodeling, skeletal pain,
855 and sprouting of sensory nerve fibers. J Pain 12:698-711.
856 Bouxsein ML, Boyd SK, Christiansen BA, Guldberg RE, Jepsen KJ, Müller R (2010) Guidelines for assessment
857 of bone microstructure in rodents using micro-computed tomography. Journal of bone and mineral
858 research : the official journal of the American Society for Bone and Mineral Research 25:1468-1486.
859 Boyer NP, Gupton SL (2018) Revisiting Netrin-1: One Who Guides (Axons). Front Cell Neurosci 12:221.
860 Bushnell B BBMAP. In. https://sourceforge.net/projects/bbmap/: SourceForge.
861 Chartier SR, Mitchell SA, Majuta LA, Mantyh PW (2018) The changing sensory and sympathetic innervation
862 of the young, adult and aging mouse femur. Neuroscience 387:178-190.
863 Chen G, Zhang Y-Q, Qadri YJ, Serhan CN, Ji R-R (2018) Microglia in Pain: Detrimental and Protective Roles in
864 Pathogenesis and Resolution of Pain. Neuron 100:1292-1311.
865 Coluzzi F, Rolke R, Mercadante S (2019) Pain Management in Patients with Multiple Myeloma: An Update.
866 Cancers 11:2037.
867 Cunningham F et al. (2021) Ensembl 2022. Nucleic Acids Research 50:D988-D995.
868 Dai M, Wang P, Boyd AD, Kostov G, Athey B, Jones EG, Bunney WE, Myers RM, Speed TP, Akil H, Watson SJ,
869 Meng F (2005) Evolving gene/transcript definitions significantly alter the interpretation of GeneChip
870 data. Nucleic Acids Research 33:e175-e175.
871 Davis S, Meltzer PS (2007) GEOquery: a bridge between the Gene Expression Omnibus (GEO) and
872 BioConductor. Bioinformatics 23:1846-1847.
873 Deacon RM (2006) Burrowing in rodents: a sensitive method for detecting behavioral dysfunction. Nature
874 protocols 1:118-121.
875 Devor M, Wall PD (1976) Type of sensory nerve fibre sprouting to form a neuroma. Nature 262:705-708.
876 Diaz-delCastillo M, Hansen RB, Appel CK, Nielsen L, Nielsen SN, Karyniotakis K, Dahl LM, Andreasen RB,
877 Heegaard A-M (2020a) Modulation of Rat Cancer-Induced Bone Pain is Independent of Spinal
878 Microglia Activity. Cancers 12:2740.
879 Diaz-delCastillo M, Kamstrup D, Olsen RB, Hansen RB, Pembridge T, Simanskaite B, Jimenez-Andrade JM,
880 Lawson MA, Heegaard AM (2020b) Differential Pain-Related Behaviors and Bone Disease in
881 Immunocompetent Mouse Models of Myeloma. JBMR Plus 4:e10252.
882 Diaz-delCastillo M, Kamstrup D, Olsen R, Hansen R, Pembridge T, Simanskaite B, Andrade-Jimenez J, Lawson
883 M, Heegaard AM (2019) Differential pain-related behaviours and bone disease in immunocompetent
884 mouse models of myeloma. JBMR Plus.
885 Dickenman RC, Chason JL (1958) Alterations in the dorsal root ganglia and adjacent nerves in the leukemias,
886 the lymphomas and multiple myeloma. Am J Pathol 34:349-361.
887 Dong M, Zhang J, Han X, He J, Zheng G, Cai Z (2022) Baseline peripheral neuropathy was associated with age
888 and a prognostic factor in newly diagnosed multiple myeloma patients. Scientific Reports 12:10061.
889 Dun X-P, Parkinson DB (2017) Role of Netrin-1 Signaling in Nerve Regeneration. International Journal of
890 Molecular Sciences 18:491.
891 Fahed D, Chettab A, Mathe D, Denis M, Traverse-Glehen A, Karlin L, Perrial E, Dumontet C (2022) Netrin-1
892 expression and targeting in multiple myeloma. Leuk Lymphoma 63:395-403.
893 Frankish A, Diekhans M, Ferreira A-M, Johnson R, Jungreis I, Loveland J, Mudge JM, Sisu C, Wright J,
894 Armstrong J (2019) GENCODE reference annotation for the human and mouse genomes. Nucleic
895 acids research 47:D766-D773.
896 Ghilardi JR, Freeman KT, Jimenez-Andrade JM, Mantyh WG, Bloom AP, Kuskowski MA, Mantyh PW (2010)
897 Administration of a tropomyosin receptor kinase inhibitor attenuates sarcoma-induced nerve
898 sprouting, neuroma formation and bone cancer pain. Mol Pain 6:87.

899 Glaser J, Gonzalez R, Perreau VM, Cotman CW, Keirstead HS (2004) Neutralization of the chemokine CXCL10
900 enhances tissue sparing and angiogenesis following spinal cord injury. J Neurosci Res 77:701-708.
901 Hiasa M, Okui T, Allette YM, Ripsch MS, Sun-Wada GH, Wakabayashi H, Roodman GD, White FA, Yoneda T
902 (2017) Bone pain induced by multiple myeloma is reduced by targeting V-ATPase and ASIC3. Cancer
903 research 77:1283-1295.
904 Hirakawa H, Okajima S, Nagaoka T, Kubo T, Takamatsu T, Oyamada M (2004) Regional differences in blood-
905 nerve barrier function and tight-junction protein expression within the rat dorsal root ganglion.
906 Neuroreport 15:405-408.
907 Honore P, Rogers SD, Schwei MJ, Salak-Johnson JL, Luger NM, Sabino MC, Clohisy DR, Mantyh PW (2000)
908 Murine models of inflammatory, neuropathic and cancer pain each generates a unique set of
909 neurochemical changes in the spinal cord and sensory neurons. Neuroscience 98:585-598.
910 Howe KL et al. (2020) Ensembl 2021. Nucleic Acids Research 49:D884-D891.
911 Inoue K, Tsuda M (2018) Microglia in neuropathic pain: cellular and molecular mechanisms and therapeutic
912 potential. Nat Rev Neurosci 19:138-152.
913 Ireland WP, Fletcher TF, Bingham C (1981) Quantification of microvasculature in the canine spinal cord. The
914 Anatomical record 200:102-113.
915 Jang JS, Li Y, Mitra AK, Bi L, Abyzov A, van Wijnen AJ, Baughn LB, Van Ness B, Rajkumar V, Kumar S, Jen J
916 (2019) Molecular signatures of multiple myeloma progression through single cell RNA-Seq. Blood
917 Cancer J 9:2.
918 Jimenez-Andrade JM, Herrera MB, Ghilardi JR, Vardanyan M, Melemedjian OK, Mantyh PW (2008)
919 Vascularization of the dorsal root ganglia and peripheral nerve of the mouse: implications for
920 chemical-induced peripheral sensory neuropathies. Mol Pain 4:10.
921 Jimenez-Andrade JM, Bloom AP, Stake JI, Mantyh WG, Taylor RN, Freeman KT, Ghilardi JR, Kuskowski MA,
922 Mantyh PW (2010) Pathological sprouting of adult nociceptors in chronic prostate cancer-induced
923 bone pain. Journal of Neuroscience 30:14649-14656.
924 Johnsen AT, Tholstrup D, Petersen MA, Pedersen L, Groenvold M (2009) Health related quality of life in a
925 nationally representative sample of haematological patients. European journal of haematology
926 83:139-148.
927 Kazandjian D, Landgren O (2016) A look backward and forward in the regulatory and treatment history of
928 multiple myeloma: approval of novel-novel agents, new drug development, and longer patient
929 survival. In: Seminars in oncology, pp 682-689: Elsevier.
930 Kumar SK, Rajkumar SV, Dispenzieri A, Lacy MQ, Hayman SR, Buadi FK, Zeldenrust SR, Dingli D, Russell SJ, Lust
931 JA, Greipp PR, Kyle RA, Gertz MA (2008) Improved survival in multiple myeloma and the impact of
932 novel therapies. Blood 111:2516-2520.
933 Kyle RA, Rajkumar SV (2009) Criteria for diagnosis, staging, risk stratification and response assessment of
934 multiple myeloma. Leukemia 23:3-9.
935 Lawson MA, Paton-Hough JM, Evans HR, Walker RE, Harris W, Ratnabalan D, Snowden JA, Chantry AD (2015)
936 NOD/SCID-GAMMA mice are an ideal strain to assess the efficacy of therapeutic agents used in the
937 treatment of myeloma bone disease. PLoS One 10:e0119546.
938 Love MI, Huber W, Anders S (2014) Moderated estimation of fold change and dispersion for RNA-seq data
939 with DESeq2. Genome Biol 15:550.
940 Mach DB, Rogers SD, Sabino MC, Luger NM, Schwei MJ, Pomonis JD, Keyser CP, Clohisy DR, Adams DJ, O'Leary
941 P, Mantyh PW (2002) Origins of skeletal pain: sensory and sympathetic innervation of the mouse
942 femur. Neuroscience 113:155-166.
943 Madison RD, Zomorodi A, Robinson GA (2000) Netrin-1 and peripheral nerve regeneration in the adult rat.
944 Experimental neurology 161:563-570.
945 Mantyh PW (2014) The neurobiology of skeletal pain. Eur J Neurosci 39:508-519.
946 Mantyh WG, Jimenez-Andrade JM, Stake JI, Bloom AP, Kaczmarska MJ, Taylor RN, Freeman KT, Ghilardi JR,
947 Kuskowski MA, Mantyh PW (2010) Blockade of nerve sprouting and neuroma formation markedly
948 attenuates the development of late stage cancer pain. Neuroscience 171:588-598.
949 Martin CD, Jimenez-Andrade JM, Ghilardi JR, Mantyh PW (2007) Organization of a unique net-like meshwork
950 of CGRP+ sensory fibers in the mouse periosteum: Implications for the generation and maintenance
951 of bone fracture pain. Neuroscience Letters 427:148-152.

952 Mercadante S (2018) Treating breakthrough pain in oncology. Expert review of anticancer therapy 18:445-
953 449.
954 Mhaskar R, Kumar A, Miladinovic B, Djulbegovic B (2017) Bisphosphonates in multiple myeloma: an updated
955 network meta-analysis. The Cochrane database of systematic reviews 12:Cd003188.
956 Niscola P, Scaramucci L, Romani C, Giovannini M, Tendas A, Brunetti G, Cartoni C, Palumbo R, Vischini G,
957 Siniscalchi A, de Fabritiis P, Caravita T (2010) Pain management in multiple myeloma. Expert review
958 of anticancer therapy 10:415-425.
959 Olechnowicz SWZ, Weivoda MM, Lwin ST, Leung SK, Gooding S, Nador G, Javaid MK, Ramasamy K, Rao SR,
960 Edwards JR, Edwards CM (2019) Multiple myeloma increases nerve growth factor and other pain-
961 related markers through interactions with the bone microenvironment. Scientific Reports 9:14189.
962 Oortgiesen BE, Kroes JA, Scholtens P, Hoogland J, Dannenberg - de Keijzer P, Siemes C, Jansman FGA,
963 Kibbelaar RE, Veeger NJGM, Hoogendoorn M, van Roon EN (2022) High prevalence of peripheral
964 neuropathy in multiple myeloma patients and the impact of vitamin D levels, a cross-sectional study.
965 Supportive Care in Cancer 30:271-278.
966 Patro R, Duggal G, Love MI, Irizarry RA, Kingsford C (2017) Salmon provides fast and bias-aware quantification
967 of transcript expression. Nature Methods 14:417-419.
968 Peters CM, Jimenez-Andrade JM, Kuskowski MA, Ghilardi JR, Mantyh PW (2007) An evolving cellular
969 pathology occurs in dorsal root ganglia, peripheral nerve and spinal cord following intravenous
970 administration of paclitaxel in the rat. Brain Res 1168:46-59.
971 Peters CM, Ghilardi JR, Keyser CP, Kubota K, Lindsay TH, Luger NM, Mach DB, Schwei MJ, Sevcik MA, Mantyh
972 PW (2005) Tumor-induced injury of primary afferent sensory nerve fibers in bone cancer pain. Exp
973 Neurol 193:85-100.
974 Porta-Sales J, Garzón-Rodríguez C, Llorens-Torromé S, Brunelli C, Pigni A, Caraceni A (2017) Evidence on the
975 analgesic role of bisphosphonates and denosumab in the treatment of pain due to bone metastases:
976 A systematic review within the European Association for Palliative Care guidelines project. Palliative
977 medicine 31:5-25.
978 Quinn B, Ludwig H, Bailey A, Khela K, Marongiu A, Carlson KB, Rider A, Seesaghur A (2022) Physical, emotional
979 and social pain communication by patients diagnosed and living with multiple myeloma. Pain
980 management 12:59-74.
981 Ramsenthaler C, Kane P, Gao W, Siegert RJ, Edmonds PM, Schey SA, Higginson IJ (2016) Prevalence of
982 symptoms in patients with multiple myeloma: a systematic review and meta-analysis. European
983 journal of haematology 97:416-429.
984 Ray P, Torck A, Quigley L, Wangzhou A, Neiman M, Rao C, Lam T, Kim JY, Kim TH, Zhang MQ, Dussor G, Price
985 TJ (2018) Comparative transcriptome profiling of the human and mouse dorsal root ganglia: an RNA-
986 seq-based resource for pain and sensory neuroscience research. Pain 159:1325-1345.
987 Ray PR, Shiers S, Caruso JP, Tavares-Ferreira D, Sankaranarayanan I, Uhelski ML, Li Y, North RY, Tatsui C,
988 Dussor G, Burton MD, Dougherty PM, Price TJ (2022) RNA profiling of human dorsal root ganglia
989 reveals sex-differences in mechanisms promoting neuropathic pain. Brain.
990 Richardson PG et al. (2012) Management of treatment-emergent peripheral neuropathy in multiple
991 myeloma. Leukemia 26:595-608.
992 Rudjito R, Agalave NM, Farinotti AB, Baharpoor A, Martinez Martinez A, Islas EM, Panwar P, Brömme D,
993 Barbier J, Marchand F, Mehlen P, Andersen TL, Andrade JMJ, Svensson CI (2021) Bone innervation
994 and vascularization regulated by osteoclasts contribute to refractive pain-related behavior in the
995 collagen antibody-induced arthritis model. bioRxiv:2021.2004.2019.440384.
996 Sacks D et al. (2018) Multisociety Consensus Quality Improvement Revised Consensus Statement for
997 Endovascular Therapy of Acute Ischemic Stroke. Int J Stroke 13:612-632.
998 Sayilekshmy M, Hansen RB, Delaisse JM, Rolighed L, Andersen TL, Heegaard AM (2019) Innervation is higher
999 above Bone Remodeling Surfaces and in Cortical Pores in Human Bone: Lessons from patients with
1000 primary hyperparathyroidism. Sci Rep 9:5361.
1001 Sliepen SHJ, Diaz-Delcastillo M, Korioth J, Olsen RB, Appel CK, Christoph T, Heegaard A-M, Rutten K (2019)
1002 Cancer-induced Bone Pain Impairs Burrowing Behaviour in Mouse and Rat. In vivo (Athens, Greece)
1003 33:1125-1132.
1004 SnapGene In. Dotmatics.

1005 Soneson C, Love MI, Robinson MD (2015) Differential analyses for RNA-seq: transcript-level estimates
1006 improve gene-level inferences. F1000Res 4:1521.
1007 Sopata M, Katz N, Carey W, Smith MD, Keller D, Verburg KM, West CR, Wolfram G, Brown MT (2015) Efficacy
1008 and safety of tanezumab in the treatment of pain from bone metastases. Pain 156:1703-1713.
1009 Sung JH, Mastri AR (1983) Aberrant peripheral nerves and microneuromas in otherwise normal medullas. J
1010 Neuropathol Exp Neurol 42:522-528.
1011 Weidner N, Semple JP, Welch WR, Folkman J (1991) Tumor angiogenesis and metastasis--correlation in
1012 invasive breast carcinoma. N Engl J Med 324:1-8.
1013 Yu G (2019) Enrichplot: visualization of functional enrichment result. R package version 1.
1014 Yu G, He QY (2016) ReactomePA: an R/Bioconductor package for reactome pathway analysis and
1015 visualization. Mol Biosyst 12:477-479.
1016 Yu G, Wang LG, Yan GR, He QY (2015) DOSE: an R/Bioconductor package for disease ontology semantic and
1017 enrichment analysis. Bioinformatics 31:608-609.
1018 Zhan F, Huang Y, Colla S, Stewart JP, Hanamura I, Gupta S, Epstein J, Yaccoby S, Sawyer J, Burington B, Anaissie
1019 E, Hollmig K, Pineda-Roman M, Tricot G, van Rhee F, Walker R, Zangari M, Crowley J, Barlogie B,
1020 Shaughnessy JD, Jr. (2006) The molecular classification of multiple myeloma. Blood 108:2020-2028.
1021 Zheng B, Li S, Xiang Y, Zong W, Ma Q, Wang S, Wu H, Song H, Ren H, Chen J (2023) Netrin-1 mediates nerve
1022 innervation and angiogenesis leading to discogenic pain. Journal of Orthopaedic Translation 39:21-
1023 33.
1024 Zhu S, Zhu J, Zhen G, Hu Y, An S, Li Y, Zheng Q, Chen Z, Yang Y, Wan M (2019) Subchondral bone osteoclasts
1025 induce sensory innervation and osteoarthritis pain. The Journal of clinical investigation 129:1076-
1026 1093.

1027